REVIEW 2

Radiation damage in biotite mica by accelerated α-particles: a synchrotron microfocus X-ray diffraction and X-ray absorption spectroscopy study

WILLIAM R. BOWER[1*], CAROLYN I. PEARCE[2], ANDREW D. SMITH[3], SIMON M. PIMBLOTT[3], J. FREDERICK W. MOSSELMANS[4], SARAH J. HAIGH[5], JAMES P. McKINLEY[6], RICHARD A.D. PATTRICK[1]

[1]Research Centre for Radwaste Disposal & Williamson Research Centre, School of Earth, Atmospheric and Environmental Science, The University of Manchester, M13 9PL, UK
[2]Dalton Nuclear Institute & School of Chemistry, The University of Manchester, M13 9PL UK
[3]Dalton Cumbrian Facility, Dalton Nuclear Institute, Westlakes Science Park, CA24 3HA, UK
[4]Diamond Light Source, Harwell, OX11 0QX, UK
[5]School of Materials, University of Manchester, M13 9PL, UK
[6]Pacific Northwestern National Laboratory, Richland, WA, 99354, USA

Corresponding author email: william.bower@manchester.ac.uk

Keywords: radiation damage, phyllosilicates, biotite, α-particle, pelletron, irradiation, synchrotron, microfocus, X-ray diffraction, X-ray absorption, EXAFS, infrared, spectroscopy, geodisposal, nuclear waste

ABSTRACT

A critical radiation damage assessment of the materials that will be present in a Geological Disposal Facility (GDF) for radioactive waste is a priority for building a safety case. Detailed analysis of the effects of high energy α-particle damage in phyllosilicates such as mica is a necessity, as these are model structures for both the clay-based backfill material and the highly sorbent components of a crystalline host rock. The α-radiation stability of biotite mica (general formula: $K(Mg,Fe)_3(Al,Si_3O_{10})(F,OH)_2$) has been investigated using the 5 MV tandem pelletron at the University of Manchester's Dalton Cumbrian Facility (DCF) and both the microfocus spectroscopy (I18) and core X-ray absorption spectroscopy (B18) beamlines at Diamond Light Source (UK). Microfocus X-ray diffraction 'mapping' has demonstrated extensive structural aberrations in the mica resulting from controlled exposure to the focused $^4He^{2+}$ ion (α-particle) beam. Delivered doses were comparable to α-particle fluences expected in the highly active, near-field of a GDF. At doses up to 6.77 displacements per atom (dpa) in the region of highest particle fluence, biotite mica displays a heterogeneous structural response to irradiation on a micron scale, with sequential dilation and contraction of regions of the structure perpendicular to the sheets, as well as a general overall contraction of the phyllosilicate layer spacing. At the peak of ion fluence, the structure collapses under a high point defect density and amorphous areas are pervasive amongst altered domains of the original lattice. Such structural alterations are likely to affect the material's capacity to sorb and retain escaped radionuclides over long time scales; increased edge site availability may favour increased sorption whilst interlayer uptake will likely be reduced due to collapse. Radiation-induced reduction of structural iron at the region of highest structural damage across an α-particle's track has been demonstrated by Fe *K*-edge X-ray absorption near edge spectroscopy (XANES) and local structural disorder has been confirmed by analysis of both potassium *K*-edge XANES and Fe *K*-edge extended X-ray absorption fine structure analysis. An infra-red absorption study of deformations in the OH^- stretching region, along with electronprobe microanalysis complements the synchrotron data presented here.

INTRODUCTION

Phyllosilicates, such as mica and clay mineral phases, are of critical importance to the international safety case behind the construction of a long-term geological disposal facility (GDF) for radioactive waste. Biotite is a ubiquitous component of the crystalline host rocks being considered for permanent geological isolation and phyllosilicate structures are expected to retard radionuclide transport following eventual waste canister failure, accumulating radiation damage in the process. In addition, mica shares similar structural and chemical characteristics with components of the proposed bentonite backfill (i.e. hydrated, metal rich layer-silicates with variable interlayer components) and an investigation into the α-radiation stability of biotite will have important parallels for clay-based barrier performance assessment in a repository (Lee and Tank, 1985; Allard and Calas, 2009; Savage and Arthur, 2012). An examination of the effects of ionising radiation on these mineral structures and the potential impact upon their durability as barrier materials is essential.

The microscale, naturally occurring radiation damage accumulation in biotite mica by α-particles has been studied before. Commonly exhibiting darkened aureoles of α-radiation damage surrounding micrometer-scale radioactive inclusions, biotite is a useful proxy for studying the complex, heterogeneous nature of radiation damage in layered minerals over long timescales (Nasdala et al., 2001, 2006; Pattrick et al., 2013; Bower et al., 2015b). This study presents the results of controlled α-radiation damage in biotite mica using accelerated (5 MeV) $^{4}He^{2+}$ ions to systematically examine the effects of α-particle bombardment on the mineral structure and chemistry. With control over the ion energy, flux and sample irradiation conditions, elucidating the mechanisms of radiation damage is possible, in contrast to naturally radiation damaged samples which may have unconstrained thermal histories. α-particles are identical to $^{4}He^{2+}$ ions, however $^{4}He^{2+}$ ions are conventionally termed 'alpha' particles only when they are a product of nuclear decay (Lieser, 1997). For the purposes of this study, both α-particles and $^{4}He^{2+}$ ions are considered synonymous.

METHODS

Biotite Mica

The biotite samples irradiated in this study were extracted from a large (10 x 15 x 0.5 cm) single crystal from Iveland, Southern Norway (Rickwood, 1981), displaying chemical homogeneity across broad (cm scale) areas. Electron probe microanalysis (EPMA) yielded an average formula of $K_{0.83}Na_{0.016}(Mg+Fe_{1.21})Ti_{0.17}Al_{1.13}Si_{2.60}O_{10}(F,OH)_2$ where Mg/(Mg+Fe)=0.545, siting the biotite near the centre of the phlogopite-annite solid solution series. For the purposes of this study, the term 'biotite' is employed to describe the sample, albeit it is a general series name for trioctahedral dark mica (Rieder et al., 1999).

The biotite mica structure comprises sheets of metal rich octahedra (O), bounded by silica and alumina rich sheets of tetrahedra (T) arranged in hexagonal rings; the apical oxygens of the tetrahedral layers point inwards towards the octahedral layer. Biotite is a trioctahedral mica, indicating that all three octahedral sites are occupied, however vacant sites are typical across the structure (Fleet et al., 2003). Negatively charged TOT sheets are weakly bonded by interlayer potassium cations, a minor lateral offset in sheet stacking results in a monoclinic crystal habit. Structural hydroxyl groups lie in the centre of the hexagonal tetrahedral rings (see Figure 1). Such 2:1 phyllosilicates are typified by their perfect (001) cleavage, easily splitting along interlayers.

Ion irradiation

Samples were irradiated using the University of Manchester's newly commissioned 5 MV NEC 15SDH-4 tandem pelletron ion accelerator, equipped with a toroidal volume ion source (TORVIS) at the Dalton Cumbrian Facility, UK (Leay et al., 2014). Samples were held in a customized target station (Bower et al., 2015) and irradiated under vacuum with a focused $^{4}He^{2+}$ beam. The energy of the ion beam on the sample was held at 5 MeV across all exposures, in line with α-particle energies along the uranium decay chains (48 MeV) (see NNDC, 2013). Activation cross-sections were calculated for incident helium ions accelerated into constituent elements of the biotite target chemistry

to ensure any activation of the mica would be kept as low as reasonably possible. An incident energy of 5 MeV was therefore selected to minimise sample activation. Ion fluences were varied with irradiation time and beam current, which was kept sufficiently low (< 300 nA) to minimise the temperature increase on samples during exposure. Biotite samples were prepared as thin (< 40 μm) cleavage parallel planes and mounted on glass slides for irradiation. As such, samples were irradiated along a plane normal to (001), perpendicular to the phyllosilicate layers (see Figure 1). Post-exposure, samples were further thinned (by peeling along the {001} cleavage) from the back to remove the undamaged material and isolate the high defect density layer for analysis.

Ion dose and radiation damage modeling

Radiation damage in materials is expressed in units of displacements per atom (dpa) i.e. a dpa value of 0.1 signifies that 10% of the atoms in the structure have been displaced from their original sites at least once. The Monte-Carlo based simulation software, the Stopping and Range of Ions in Matter (SRIM) (Ziegler, 2013) was used to calculate necessary ion fluences to achieve sequentially increasing ion doses across the biotite samples, up to a maximum ion density normalised dose of 6.77 dpa (average across dose gradient = 0.28 dpa; see Tables 1 & 2). The critical amorphisation threshold for a mica structure has been calculated to be 0.15 dpa (Wang et al. 1998), however the X-ray diffraction (XRD) study here demonstrates that some original structure is retained at doses far higher than this, despite extensive point defect densities throughout the former lattice. SRIM modeling was used to determine that a relatively light incident ion such as helium entering a mica sample at 5 MeV creates on average 225 knock-on displacements (Frenkel defects) per ion track in the sample. Across such a track, the interaction of the ions with the biotite displays a peak with respect to atomic displacements at ca. 18 μm from sample surface. Energy is lost via ionisation through the region of low nuclear interaction i.e. the first ~15 μm as the α-particle accepts electrons to render it a neutral helium atom. For comparison, SRIM modeling using 8 MeV helium ions indicated an average of 249 'knock-on' displacements over a 36 μm ion track, thus an increase in ion energy does not denote a proportional increase in radiation damage, as structural interaction is theoretically maximised only after sufficient energy is lost to ionisation (helium ion energy ~ 100 keV or less).

Three biotite samples exposed to sequentially increasing ion doses have been analysed in this study (Table 1). Across all samples, >97 % of the beam fluence was contained within $1cm^2$.

Beam intensity using the DCF Pelletron's focused ion beam displays a Gaussian profile in real space with respect to particle fluence. In this manner, one sample can accumulate a range of doses along a beam radius of ~ 6.75 mm and thereby allow analysis of relative changes in damage accumulation across a single sample (see Figure 2). The ion fluence gradient across the beam spot for Sample 1, and the corresponding estimates of dpa values based on the integrated ion beam densities at intervals across the profile are given in Table 2.

Placed in broad context for a deep geological disposal facility, Reed et al., (1987) calculate that within a high level waste repository, the total absorbed α-dose at the surface of a waste package will be ~ $1.4x10^8$ gray. This model assumes a 10,000 year integration time and canister failure after 1000 years. In comparison, the total α-dose across sample 1 (Table 1), surface-area normalized for Reed et al.,'s calculations, equates to ~$1.5x10^6$ gray; samples 2 and 3 received $0.9x10^6$ and $0.3x10^9$ gray respectively. These doses are a large over estimate for that predicted to be experienced by the far-field host rock, however the parallels between phyllosilicates and bentonite backfill constituent minerals make this dose a reasonable proxy for near-canister materials, although not as high as the modeled surficial dose under the assumptions presented by the 1987 study. Further work at higher doses is currently underway. The concentration of radionuclides in a host rock following release must also be considered (through fluid flow and sorption onto host rock constituents/precipitation of radionuclide bearing phases) and may cause variations in expected doses in the far field. A 10,000 year model is rather short; it is likely than in the near field, the host rock will be subject to radiation fields up to 100,000 years and radionuclides will be concentrated in specific locations, such as phyllosilicates in permeable zones.

Synchrotron analysis

Structural and chemical analysis of the radiation damaged samples was undertaken on beamlines I18 and B18, Diamond Light Source, UK (Dent et al. 2009; Mosselmans et al. 2009).

Microfocus X-ray diffraction

Microfocus, high resolution X-ray diffraction (μXRD) patterns were collected in transmission imaging mode on beamline I18, with a beam energy of 12 keV and a spot size of ~ 3 μm diameter. The setup comprised a Photonic Science XDI-VHR 125 CCD ranging from 12-44° 2θ with image acquisition times of ca. 10-30s, depending on sample thickness. Si powder was used to calibrate the images. The software Igor Pro (Igor Pro, 2014) with the Nika plugin (Ilavsky, 2012) was used to calibrate and reduce the diffraction data and MatLab (The MathWorks Inc. 2013) was used to compile μXRD 'maps'.

Sequential μXRD traverses across the $^{4}He^{2+}$ ion beam dose gradient have quantified changes in the structural parameters of biotite mica with increasing radiation damage. The irradiated samples were mounted relative to the X-ray beam in two orientations; one with a 10° offset from [001] (z-axis parallel) and another with a similar offset from [100] (x-axis parallel) to yield information from both normal to and parallel to the basal plane, respectively. In this way, structural analysis could be performed both along the irradiation vector and also at 90° to this, the latter permitting analysis of the depth of the ions' penetration into the sample. A high-precision XY stage was used to trace the beam across damaged regions; for the purposes of these experiments, a beam step size of between 5-30 μm was used, depending on required resolution.

Cu Kα (1.541 Å) diffraction peaks for the biotite crystal structure were modelled using the software *Jems* (Stadelmann, 2012) and comparisons made with the synchrotron XRD peaks at 12 keV (1.033 Å). Where confident identification was possible, indexed peaks have been quoted within diffraction patterns. Reduced diffraction patterns have been fitted with a combination of Gaussian and Voigt line profiles to give more accurate peak positions in 2θ space.

Microfocus X-ray absorption spectroscopy

X-ray absorption spectroscopy (XAS) data were acquired at both the Fe and K *K*-edges across the radiation damaged samples, yielding information on the oxidation state and short range structure of the Fe-rich octahedral layers, as well as the local structure of the K-rich interlayers, respectively. Microfocus, Fe *K*-edge XAS data were collected in fluorescence mode on beamline I18, along traverses coincident with XRD data acquisition. The penetration depth of the X-rays at the Fe *K*-edge is ~ 20 μm given the chemistry and density of the sample, this is broadly consistent with the modeled penetration distance of the α-particles into biotite, thus a useful probe for the region of highest structural damage across the α-particle's track. Given its lower edge energy, potassium data was sampled from a shallower region (~ 10 μm from the surface). Potassium *K*-edge XANES data were also collected in fluorescence mode in a helium atmosphere on beamline B18, the core extended X-ray absorption fine structure (EXAFS) beamline at Diamond Light Source. In contrast to the microfocus (~ 3 μm spot size) study, beamline B18 acquires an average signal from a broad area (~ 1 mm spot size) of sample. All XAS data were reduced and analysed with the *Demeter* suite (Ravel and Newville, 2005). Spectra are presented as background subtracted, intensity normalized plots. In the instance of the potassium data, multiple (~16 per sample) spectra have been merged to yield better data quality.

Fourier transform infra-red spectroscopy

Fourier transform infra-red (FT-IR) spectra were collected using a Spotlight™ 400 FT-IR spectrometer in attenuated total reflectance (ATR) mode. Single cleavage planes of biotite were placed flat against the ATR crystal and scanned in high resolution across the characteristic absorption window for the OH^- stretching region (3800-3300cm^{-1}). Spectra were reduced and normalized in the specialist FT-IR analysis software OMNIC (Thermo Electron Corporation, 2004).

Electronprobe microanalysis

Electronprobe microanalysis (EPMA) was undertaken using the Pacific Northwestern National Laboratory's (PNNL) JEOL 8200. The instrument was calibrated against commercial P&H Developments mineral standards: albite ($NaAlSi_3O_8$), apatite $Ca_5(PO_4)_3(OH,F,Cl)$, hematite (Fe_2O_3), periclase (MgO), orthoclase ($KAlSi_3O_8$), rutile (TiO_2) and wollastonite ($CaSiO_3$).

RESULTS AND DISCUSSION

Microfocus XRD

Analysis perpendicular to basal plane (z-axis parallel)

Two XRD traverses across sample 1 are presented in the following section (Figures 4-8). Initially, a series of images were collected from the undamaged region into the zone of maximum ion dose with an image acquisition step of 30 µm (233 patterns over 7000 µm) (Figures 3 & 4 i-iii). This was complimented by a shorter, higher resolution traverse with a step size of 5 µm across a 300-µm region of interest (60 patterns), selected to display a representative area of diffraction peak variability (Figure 4 iv). Both sets of diffraction patterns were collected along the Gaussian profile of the ion fluence gradient shown in Figure 2. Representative CCD images from sequential positions across the irradiated biotite are displayed in Figure 3.

At 7000 µm from the ion beam fluence maximum, the area analysed is outside the irradiated region and sharp spots are visible in the diffraction pattern (Figure 3). Crossing over the ion beam limit, minor reflection angle fluctuations and some diminished intensity occurs until ca. 4000 µm from the peak of ion dose, however, the original structure is still evident and all reflections are represented by sharp spots. At 4000 µm some diffraction spots have split and most high angle reflections have become more diffuse. Peak splitting, line broadening and selective intensity reduction persist to 2000 µm, whereupon spots become smeared, inconsistent rings; indicative of multiple crystallites of this pseudo-original structure in numerous orientations. Where the ion beam dose was highest (1000 µm

to 0 μm), nearly all reflections have disappeared and the resulting pattern is a series of highly diffuse, minor reflections bearing only a slight resemblance to the original structure. The biotite is interpreted to be extensively amorphous over the final ~ 500 μm towards the beam centre, as broad, diffuse spots become faint, minor reflections, signifying near complete loss of long range order.

Merging a series of 1D patterns (reduced via rotational averaging of the CCD images) yields the XRD 'map' shown in Figure 4. The diffraction map has been separated into three regions of interest for subsequent discussion. Panel i is the lowest dose region and displays the reflections outside the irradiated area as well as the limit of the ion beam. Consequently, at this scale, reflections show both unirradiated and irradiated regions and thus a high reflection angle variability. Panel ii is a region of more intense dose across the Gaussian gradient whereby radiation effects are more pervasive. Panel iii therefore represents the peak of ion dose across the biotite and is dominated by near-amorphous regions.

Several assertions can be made from detailed analysis of these maps. Relative comparisons in XRD patterns have been made across a single sample, owing to the difficulty in indexing patterns across multiple single crystals using microfocus diffraction due to orientation and thickness variations. Panel i (7000 μm – 4700 μm) shows a higher variation in 2θ values than any other point across the traverse at this scale. Directly across the ion beam limit, most reflections shift to higher angles (lower d-spacings) by up to 2 degrees 2θ and broaden, periodically fluctuating back towards their original values. The line broadening observed is consistent with a contribution from point defect accumulation, however there is no apparent peak splitting or loss of reflections in the initial low dose area. It is likely that at these doses, radiation damage in the crystal is variable in intensity due to the stochasticity of defect accumulation in the sample, thus lattice dimensions are extremely heterogeneous on a micron scale. The map suggests areas of undamaged crystal are neighbouring regions where bulk crystal parameters have shifted slightly (collapsed) to accommodate increased point defects. Across the region of highest ion beam damage within panel i, most peaks have moved

to higher 2θ values and these peak positions remain relatively constant, indicating increasing defect concentrations throughout the crystal, yielding a more homogeneous bulk structural response to irradiation.

Panel ii (4700 μm – 2200 μm from peak of dose) displays a new reflection (also visible in the top of panel i, ca. 5200 μm from the peak of ion dose), 'growing in' at ca. 24.9 degrees 2θ. This 'new' peak, indexed as the biotite (158) reflection, remains the most intense reflection across the traverse as the dose the biotite experienced increases. The emergence of this peak is consistent with the introduction of rings in the diffraction patterns. It is proposed that a further increase in point defect density results in the reorientation of crystallites within the structure, revealing new reflections in the view direction.

Of particular interest is the high resolution trace (panel iv) (~4300 μm – 4000 μm from the peak of ion dose) across panel ii, displaying significant deviations in diffraction angle with smaller peaks 'splitting' from the main reflection. These 'satellite' reflections display a sinusoidal movement in 2θ space, arcing away from and then back towards the intense, primary reflection. Peak splitting is indicative of a non-uniform structural response to higher defect accumulation and suggests the presence of multiple crystallites with varying lattice parameters. Certain sinusoids appear concomitant, moving in phase with a neighbouring reflection, whilst others have a shallower deviation from the main peak and appear out of phase as regions of the crystal dilate and contract sequentially. It is clear that radiation damage and structural accommodation have a consequential effect across neighbouring areas in the structure.

In panel iii (2200 μm - 0 μm from peak of dose), reflection intensity across all peaks has diminished and closely spaced peaks have merged and cannot be isolated for indexing. The peak at ~27° displays a large progressive increase in 2θ of up to 5° with increasing ion beam intensity, before losing intensity and becoming indistinguishable from background. Structural collapse is prevalent across the

region of highest dose and all reflections are sporadic and highly diffuse by the centre of the ion beam spot.

Figure 5 displays the reduced 1D diffraction patterns at intervals across the traverse with peaks indexed. In the context of the biotite crystal structure, reflection (131) (at ca. 22.8 degrees 2θ) denotes a plane of metal cations in alternate octahedral sheets *across* phyllosilicate layers. With increasing ion fluence, the (131) peak splits and both peaks display a shift to higher reflection angles, signifying a contraction of 'domains' of the lattice along this plane. At the peak of radiation damage, this reflection is lost, likely due to a variation in phyllosilicate layer offset such that the cations are no longer in-plane.

A contractive shift is also observed for reflection (204) (at ca. 26.9 degrees 2θ), a plane of octahedral metal cations in a similar orientation to the (131) plane, however at a more oblique angle to the basal plane. The (204) reflection splits and displays multiple satellite peaks that vary sinusoidally in real space, suggesting that structural change perpendicular to the phyllosilicate layers is non-uniform; indeed contractions along certain planes of metal cations results in corresponding expansion elsewhere in the crystal, as parts of the crystal bunch and relax to accommodate high defect densities.

Reflection (-225) (at ca. 28.8 degrees 2θ) also shifts to higher 2θ angles and represents a decrease in *d*-spacing along this plane; an oblique series of basal tetrahedral oxygens. Contraction in this plane will contribute to interlayer variations in biotite. Whilst not a contraction parallel to phyllosilicate sheets, the misalignment of basal tetrahedral atoms will cause highly variable interlayer spacing as domains within sheets become buckled.

Reflection (02,12) (at ca. 38.0 degrees 2θ) comprises planes of interlayer potassium atoms across sheets. It is clear that the interlayers are the planes most susceptible to radiation damage, as the

reflection loses nearly all intensity almost immediately across the ion beam limit. The initial loss of interlayer K^+ is in good agreement with previous studies of ion beam damaged powdered mica (Chailley et al., 1994).

The new reflection, indexed to the (158) plane in biotite, only appears with increasing $^4He^{2+}$ ion fluence (for distances < 5300 μm from the peak of ion dose). Reflection (158) represents a series of apical tetrahedral oxygen atoms in-plane across TOT layers. This region of the biotite unit cell has the highest atomic density; apical oxygens of silica tetrahedra are shared with octahedrally coordinated metal cations at the centre of the TOT sheets. Although the emergence of new reflections generally represents new phases or increased crystallization, it this is unlikely to be the case here. Whilst, most structural damage is manifested as interlayer collapse or structural offset, it is plausible to assume that metal-rich octahedral layers are the most stable element of the mica structure and that changes in layer offset will preferentially align regions with a higher percentage of crystallinity. As damage increases, crystallites of pseudo-original structure will distort to accommodate lattice strain changes; such distortions will also reveal new reflections, similar to tilting a sample in a transmission electron microscope (TEM). At the height of radiation damage, even reflection (158) has broadened and greatly diminished due to high levels of accumulated point defects. Additionally, only very minor, diffuse reflections (+/- 2 degrees from original positions) are apparent, suggesting that small domains of pseudo-original structure remain.

Relative changes in bulk lattice parameters were calculated using the X-ray diffraction analysis software *UnitCell* (Holland and Redfern, 1997), results are displayed in Figure 6. The data is refined from a series of peak-fitted patterns across points within the traverse presented in Figure 4. Only dominant, indexable reflections, rather than diffuse satellite peaks, were used in the refinement, thus small-scale changes in discrete crystallites are not represented. The biotite *a*- vector distance i.e. the shorter basal edge of the monoclinic prism (coincident with the {010} plane) only fluctuates by up to 0.1Å, thereby remaining relatively stable across the irradiated surface, only decreasing at the height of

ion fluence. This is in contrast to the *b*- vector length, which remains consistent before the ion beam limit and then becomes extremely variable with increasing radiation dose. The *b*- vector represents the long basal edge of the monoclinic prism. This variability ultimately results in a sharp decrease in unit cell volume with increasing radiation dose, as the structure collapses due to higher defect densities. Due to the orientation of the crystal upon analysis (ca. 10 degrees offset from {001}), accurate *c*-vector values were unattainable over the *z-axis parallel* XRD traverses, as no reflections yielded accurate structural information parallel to layers. Further work upon characterising interlayer behaviour is presented in the next section.

Analysis parallel to basal plane (x-axis parallel)

In comparison to the XRD analysis perpendicular to the basal plane, spectra collected parallel to the basal plane display far more reflections. Inconsistencies in interlayer arrangement mean that not all of these reflections have been accurately indexed, however a general trend can be observed across the series of representative diffraction patterns shown in Figure 7. Reflections at 0 μm denote the surface of the irradiated biotite; patterns were collected in 5μm steps along the trajectory of the incident α-particle to 30 μm, a depth which SRIM modeling predicts will be outside of the penetration depth of the 5 MeV α-particles. The highest variation in peak position occurs within 20 μm from the exposed biotite surface, although some loss in peak intensity is observed 25 μm from the surface. There is no clear indication of a zone of 'peak' radiation damage at the end of the α-particles' projected range (15 μm – 18 μm), however the data across this region is limited and peak broadening is pervasive across the traverse. The (006) reflection (at ca. 17.9 degrees 2θ), is at its most intense at the irradiated surface; this plane is one of the few elements of the structure that remains. It seems plausible to assume some level of 'packing' of the interlayers as contractive effects become pervasive, potentially retaining a certain degree of along layer crystallinity. Notably, peak (006) displays a shift to higher reflection angles, consistent with interlayer collapse.

The intensity of most reflections is diminished by the irradiated surface of the crystal and most only display an intense peak beyond 25 μm. Reflection (114) represents a series of in plane octahedral cations across the sheets; applying these trends suggests severe buckling along phyllosilicate sheets, throwing the metal cations out of plane.

Bulk X-ray diffraction across the cleavage planes was also performed on samples 2 & 3 using a Bruker D8 lab source, yielding an average interlayer signal over the entire irradiated area for comparison with unirradiated material (Figure 8). In broad agreement with the basal plane parallel analysis, the bulk analysis shows a general trend of interlayer contraction (shift to higher 2θ angles) across all layer-parallel reflections with increasing α-particle doses. Sample 3 (0.06 dpa) displays two peaks either side of the original reflection angle, indicative of the development of two main structural domains in the damaged lattice, as regions of the crystal dilate to accommodate collapse elsewhere. This trend is not continued at higher doses (sample 2, 0.18 dpa), whereupon all plane-parallel lattice planes present a contraction.

X-ray absorption spectroscopy

Fe K-edge XANES

Data collected up to 50 eV beyond the absorption edge (XANES region) yields information on the core electronic state of the absorbing atom. Figure 9 displays the Fe *K*-edges collected in both an unirradiated area (ca. 7000 μm from the ion beam centre) and an area of biotite in sample 1, calculated to have accumulated ~0.28 dpa.

The reduction of Fe(III) adds another valence electron that partially reduces the interaction between the Fe 1s electrons and the nucleus, leading to a reduced 1s binding energy and a shift of the white line to lower energies, evident in the spectrum for irradiated biotite. Clear changes in the modulations of the absorption coefficient beyond the edge are likely a product of the altered lattice dimensions

detailed earlier. Linear Combination Fitting (LCF) was possible for the two spectra presented in Figure 9, using Fe(II) and Fe(III) Fe K-edge XANES standards wüstite (FeO) and hematite (Fe_2O_3) respectively. LCF results indicate a 17.3 % increase in Fe(II) at the highest region of damage, at the depth probed by the X-rays (see supplementary information).

Fe K-edge EXAFS

At energies above the absorption edge, the 'extended' region of the spectrum gives an insight into the local environment of the absorbing atom. EXAFS data has been fitted to k=11, yielding structural information to a third coordination shell in both the unirradiated and irradiated samples, aiding quantification of radiation damage induced changes. Table 3 shows the results of the EXAFS fitting across a range of $^{4}He^{2+}$ ion doses; corresponding spectra are shown in Figure 10. Biotite mica, as a trioctahedral phyllosilicate, should have divalent ions occupying all available octahedral sites. XAS has shown that a proportion of iron is Fe(III) and that there are, therefore, local domains of dioctahedral sites within the trioctahedral layers. Vedder (1969) notes that iron rich biotites exhibit a high variability in the occupancy of octahedral layers.

Three paths have been fitted to the EXAFS spectra collected across the sample, (Fe – O), (Fe – Fe) & (Fe – Si); each path assigned a fixed coordination number with independently variable Debye-Waller factors, denoting disorder in the system. The amplitude reduction factors decrease into the irradiated region, which may suggest the fixed coordination numbers are not wholly representative of the damaged structures. Indeed, spectra C, D and E yielded better fits with reduced coordination in the second and third shells, likely a product of defects in the structure. In general there are no significant changes across the spectra, demonstrating high levels of local order at the scale analysed by EXAFS.

The irradiated spectra display a slight increase in average Fe - O distance, broadly increasing with higher doses. A Fe – O bond length increase further supports Fe(III) to Fe(II) reduction. Consistent

with the XANES linear combination fitting (see supporting information), average bond length increases across all spectra suggest up to a 20 % increase in Fe(II) across the irradiated region (at the depth probed by the X-rays).

Fe-Fe distances (equating to the distance between neighbouring octahedra in the same sheet) and coordination numbers are much more variable across the irradiated spectra. EXAFS analysis of the unirradiated biotite yields a Fe-Fe distance of 3.11 ± 0.03 Å, comparing well to previous data for biotite (Palmer and Conley, 1994). In contrast to the overall increase in Fe-O distance with irradiation, Fe-Fe distances in irradiated biotite show either a slight increase or a more substantial decrease in interatomic distance, to as low as 3.03 ± 0.03 Å. This is explained by variable, local expansion and contraction within the metal layers demonstrated by XRD. Debeye-Waller factors across the Fe-Fe scattering paths are far higher than across other paths; this may be a product of inherent 'disorder' in the octahedral layer, rather than a damage effect, as both trioctahedral and dioctahedral coordination is present in the mica structure. This may also explain why the Fe-Fe coordination number in the unirradiated sample is lower (4.7 ± 1.3) than the expected trioctahedral CN of 6, although the unirradiated values are within refinement error (Table 3).

Fitting out to the third coordination shell, Fe-Si distances (octahedrally coordinated cation to over/underlying tetrahedrally coordinated cation) show a general consistency with only small variability (+/- 0.02 Å). This suggests a general stability of T-O sheets even at high doses, with a slight contribution from within-layer collapse or buckling. The Fourier transform magnitude displays a shoulder on the peak at ~2.75 Å, although it is not present across all spectra, possibly indicative of inconsistent scattering contributions as the sheets are non-parallel. In the instances where the shoulder is not present, the contractive shift of the second shell peak is greater. The heterogeneity of damage is highlighted by the microfocus EXAFS at this resolution and it is difficult to interpret an overall trend.

K K-edge XANES

Potassium K-edge XANES data acquired on beamline B18 comprises a 'bulk' signal (beam spot = 3 mm diameter) and, therefore, provides only an average trend across a broad area of the radiation damaged samples in comparison with the undamaged material. The location and coordination of potassium in biotite presents challenges with XAS resolution. As a result, only XANES data are presented as the data produced has an insufficient k range of high enough quality to yield reasonable EXAFS fits. Figure 11 displays the potassium *K*-edge XANES and inset Fourier transforms for both unirradiated and irradiated (average over beam area ~0.28 dpa) biotite. Small changes in the local environment surrounding the potassium are evident in the irradiated sample in comparison to the unirradiated standard, as shown by slight differences in the oscillations beyond the absorption edge. A further qualitative assessment of this change is displayed in the Fourier transforms. Heterogeneous local order around the absorbing atom (i.e. inconsistencies in layer spacing even in unirradiated samples), as well as the extremely large first shell distances (~3 Å to the basal oxygens of the tetrahedral layer) yield a high background, consequently the first peak in the transform is assigned as background. The shells at ~3.2 Å and ~4.5 Å (non phase-corrected) represent basal oxygens and cations of the surrounding tetrahedral layers, respectively. Both shells display a slight shift towards shorter radial distances, in keeping with the assumption that radiation damage causes interlayer contraction. This trend has been described in previous K *K*-edge EXAFS studies of phyllomanganates (Strobel et al. 1993).

Fourier transform infra-red spectroscopy

Characteristic absorption bands across the OH^- stretching region of the biotite mica infra-red (IR) spectrum display significant changes with increasing ion fluence (Figure 12). Structural OH^- groups in mica lie in the voids at the centre of the hexagonal tetrahedral rings that make up the sheets and are oriented towards the octahedral layer (Fleet et al., 2003). Strong orientation effects are typical of this region of the mica spectrum, therefore all samples were analysed with cleavage planes perpendicular to the beam.

Importantly, the irradiated samples were analysed from the back, not from the irradiated face, as the FT-IR in ATR mode will only probe the initial 0.5-5 μm. By analysing the samples in this orientation, the modeled region of highest damage is investigated (the end of the α-particles range), broadly consistent with the region probed by synchrotron XAS. Two irradiated samples were analysed with increasing dose, as well as a sample heated in air to 110°C; the calculated maximum temperature reached over a 6 hour irradiation, to check for any thermally induced effects. Fe^{2+} oxidation through heating is a well-documented mechanism in biotite (Rancourt et al., 2001 and references therein). As no such trends were observed here, it is assumed that a sample temperature increase in-vacuum during irradiation had a negligible effect on OH^- dissociation or redox reactions.

The unirradiated biotite spectrum displays a convincing fit to model IR spectra for 'dark' mica presented by (Vedder, 1964; Wilkins, 1967; Chaussidon, 1971). A broad, intense peak at 3683cm^{-1} can be attributed to hydroxyl groups neighbouring three divalent metal ions (*N*-group bands). This region correlates to the N_C absorption band and denotes OH^- stretching neighbouring a trioctahedral (Mg^{2+} + Fe^{2+} + Fe^{2+}) coordination (Wilkins, 1967). The adjacent, lower frequency bands (two poorly defined peaks at 3585cm^{-1} and 3560cm^{-1}) denote a proposed vibration of hydroxyls adjacent to vacant sites (*V*-group bands). The lower frequency peak indexes well to the V_C band; consistent with (Fe^{3+} + Fe^{3+} + Vacancy) (Chaussidon, 1971), whilst the higher frequency peak remains unidentified.

At high $^4He^{2+}$ ion doses, significant changes are apparent. The broad, intense N_C peak has split into two maxima at 3698cm^{-1} and 3664cm^{-1}. In keeping with the Vedder (1964) and Wilkins (1967) models, these peaks index to characteristic N_B and N_D bands in biotite mica. A N_B band with a peak at 3698cm^{-1} is attributable to OH^- stretching neighbouring an (Mg^{2+} + Mg^{2+} + Mg^{2+}/Fe^{2+}) coordination, whilst a N_D band with a maximum at 3664cm^{-1} denotes a pure (Fe^{2+} + Fe^{2+} + Fe^{2+}) octahedral environment. The *V* bands become one broad peak, shifting to higher wavenumbers with increased

$^{4}He^{2+}$ ion dose, centred on 3569cm^{-1}. Shifts towards higher wavenumbers of the *V*-group bands denote an increased divalent component of the octahedral coordination i.e. (Fe^{2+} + Fe^{3+} + Vacancy).

Consistent with the XANES data, these FTIR results may be further evidence of Fe^{3+} reduction at the region of highest damage in the structure. Changes in Fe oxidation state have previously shown to yield shifts in OH^{-} stretching band frequency in clay minerals (Fialips et al. 2002). Coupled with this, the increase in intensity of the *V*-group bands denotes a higher signal from vacancy coordination, as the volume of point defects in the structure increases. It is worth noting that the observed contraction in the phyllosilicate layers as demonstrated by XRD may have an impact upon the orientation of the O-H bond, which will have a consequent impact upon absorption across the stretching region. In dioctahedral micas, the OH bond is oriented sub-normal to the (100) plane, with an inclination towards the vacant octahedral site; any increase in layer charge from the tetrahedral layer will force the bond to angle more steeply towards the octahedral layer (Fleet et al., 2003). Shifted frequencies across *V*-group bands may denote varied OH^{-} group orientation, a product of high vacancy accumulation. OH^{-} groups can act as charge transport 'bridges' between *M* sites in the octahedral layer in mica (Rosso and Ilton., 2005); reorientation and/or dissociation at high α-fluences may have detrimental consequences for electron transfer within the Fe sublattice.

Electronprobe microanalysis

Sample 1 was analysed via a step traverse from the unirradiated biotite into the discoloured damage 'zone', coincident with the X-ray diffraction traverses described in the manuscript. Table 3 shows the EMPA data across the traverse recalculated on an (OH)-free basis to 22 oxygens per formula unit (pfu). Some relatively minor chemical changes were apparent across the major elements: a slight increase in point to point variability, particularly across the Si values was present in the irradiated region (along with a notable decrease in K). Radiation damage is clearly destabilising the interlayer cations and thus Na + K will be more susceptible to volatilisation. A loss or relocation of poorly-bound Na + K may be induced by slight local heating during irradiation or indeed by EPMA analysis

(see Nielsen and Sigurdsson, 1981). However the scale of analysis of the EPMA analysis will likely not reveal the highly localised chemical changes produced by α-particle bombardment. In this sample, as in many other natural biotites, the interlayer and octahedral sites are not completely filled, and, as a result, the excess cations that are generated by treating total Fe as FeO do not exceed the stoichiometric limit of 16 pfu (Table 4), therefore it is not possible to calculate model Fe^{2+} - Fe^{3+} ratios. However, a decrease in the sum of Na + K (Table 3) into the irradiated region (ideal cation total = 2.0) may also suggest an increased Fe^{2+} component is required to retain charge balance, consistent with the XAS data.

Radiation damage mechanisms

Whilst this is the first detailed microfocus X-ray diffraction analysis of controlled α-particle radiation damage in biotite mica, some studies of swift heavy ion irradiations on similar mineral phases exist for comparison. (Chailley et al. 1994) document X-ray diffraction analysis of high energy (850 MeV) xenon and (170 MeV) oxygen irradiation of mica. Xenon irradiations yielded an overall unit cell expansion with increased defect accumulation, manifested as XRD peaks shifting to lower 2θ angles, whilst oxygen irradiations yielded only peak broadening and no overall lattice parameter change. Both this study and later work (Chailley et al., 1996) conclude the presence of 3 phases; amorphous, pseudo-crystalline and expanded phases across an irradiated mineral. Biro et al. (1997) also observed this trend using 209 MeV krypton ions, asserting that the "neutralisation" of interlayer potassium ions causes the negatively charged phyllosilicate layers to repel each other and expand. Both previous studies conclude there is a threshold of point defect accumulation below which radiation damage in mica does not affect the overall structure. These studies present the opposite structural effect to those observed with α-particles; they maintain there is an expansion of the lattice along phyllosilicate layers as a result of radiation damage. It is clear that damage manifestation with very high energy, heavy ions is wholly different than the radiation damage presented in the present study, the difference being that swift heavy ions induce multiple defect 'cascades', resulting in far higher point defect densities

along a single ion track. Comparing the differences in damage accumulation produced by heavier ions in phyllosilicates will form the basis of a future study.

Lattice contractions as a product of radiation damage have also been documented. (Lu et al. 2012) present a 1.42 % lattice contraction in cubic ZrN, manifested as a shift to higher 2θ values of XRD peaks, as a result of irradiation by 350 keV oxygen atoms. The study suggests that lower energy ions can cause unit cell contraction; the number of displacements per incident ion must be low enough such that interstitials move more readily than vacancies in a damaged structure. The migration of interstitials through a structure leaves voids (vacancy nucleation) into which the lattice collapses. Increased vacancy density thereby causes a relaxation of a crystal's inherent strain vectors. In Lu et al's example, interstitial migration is aided by the nano-scale crystal size.

Under high-fluence α-particle irradiation, both dilation and contraction are apparent *across the TOT sheets*, with extreme variability in cell parameters on a micron scale. As point defect densities increase (manifested by peak broadening), XRD analysis indicates that biotite mica forms randomly oriented crystallites of pseudo-original structure (as observed by broad 'rings' in the diffraction patterns). Such crystallites are subject to heavy distortion with increased dose, as the structure responds to the changing strain field of the increasingly damaged crystal. The likely loss of interlayer potassium from its interlayer site and coincident layer offset causes *basal plane parallel* sheet buckling and eventual structural collapse, potentially aided by the 'interstitial migration' model presented earlier (Lu et al., 2012). Of particular note is the potential for helium gas build-up in a sample, as neutral helium atoms diffuse readily through a structure and become trapped by (often self-induced) vacancies. The formation of helium 'bubbles' has been documented in plutonium metal (Wolfer 2000; Martz and Schwartz, 2003) and is likely to be a contributing factor within these samples, the presence of 'sinusoidal' movements in XRD patterns may denote periodic bubble formation at or near the surface of the biotite and such gas build up may contribute to interlayer contraction. Further work on bubble formation in these materials is underway.

Structural Fe(III) undergoes radiation-induced reduction at the region of highest structural radiation damage along an α-particle track; potentially a result of OH^- group radiolysis liberating reducing hydrogen (Pattrick et al., 2013), as well as increased electron density at depth due to displacement cascades and charge cycling by the penetrative alpha particles. Radical oxidizing species formed from hydroxyl group dissociation will be free to migrate from the structure, resulting in net reduction. In addition, the lighter oxygen atoms within this high-damage region will be more readily lost from the former lattice (largely controlled by kinetics, the probability of displacement will follow: O > Mg ~ Al > Si > Fe).

Transient displaced oxygen species, potentially leaving the structure as a neutral atom or radical anion following electron donation from the α-particles, will result in 'under coordination' of the iron (and other cations) which will be stabilized as Fe(II). It is plausible to hypothesize net chemical reduction within the discrete, highly damaged region of the α-particle's track, as increasing electron density, combined with a higher migration potential of the oxidizing species, will prevent redox balance. Oxygen displacement and loss of local order surrounding cations has been shown to be commonplace across irradiated materials (Noda et al., 1993; Moroño et al., 2009; Walsh 2011; Enterkin et al., 2011; Peuget et al. 2014a, 2014b). Whilst the Fe – O distances in the EXAFS data presented here display only a small increase, the increase is not as large as that expected for octahedrally coordinated Fe reduction. The decrease in Fe coordination by the loss of oxygen may account for this smaller than expected bond lengthening.

Net reduction may not be the sole mechanism across the entire interaction range of the α-particle; most of the analysis here has focused on the region of highest structural damage as an α-particle loses its energy towards the end of its track. Indeed, the potential for oxidation effects to dominate in the initial region of interaction, as the α-particle strips surface electrons to render it a neutral helium atom,

must also be considered. A number of mechanisms are potentially active in these damaged systems; the influence of structural water is an area of required extensive further research. Alongside the potential for radical production by OH^- radiolysis, it has been shown that the presence of water within an irradiated system can inhibit structural recovery and further promote defect concentration (Lockwood and Garofalini 2010).

Layer charge variations must also be considered, as it is highly unlikely that the radiation damaged phases are charge balanced. Increased electron density within certain regions may yield an overall higher negative charge of the TOT layers; spatial variations in layer charge may therefore also contribute to interlayer buckling, particularly if interlayer K^+ has been relocated.

Implications

With particular relevance to geological disposal, the radiation damage mechanisms presented here expose both advantages and problems for phyllosilicate performance under relatively high α-particle doses. It is apparent that mica interlayers are the most susceptible to radiation damage; this XRD study demonstrate the instability of interlayers even at low doses and it is likely that interlayer K^+ ions are liberated or relocated as a result. Such interlayer distortion will have detrimental consequences for uranium (and other radionuclides) uptake by sheet silicate minerals as contraction of the interlayer spacing below 1 nm will likely retard uptake efficiency. For example, uranium (VI) has been demonstrated to be efficiently taken up by biotite mica in the form of uranyl hydroxide (Idemitsu et al., 1995) along basal sheets, crystal edges (Ames et al., 1983) as well as within the interlayers. Phyllosilicate sheet spacing showed expansions of up to 47 % when uranyl ions were sited within mica interlayers, aided by interlayer dilation from Ca^{2+} and Na^+ substitution for K^+ (Lee et al., 2009). A consistent sheet spacing of > 1 nm is optimal for efficient uranium uptake within interlayers; such consistency is not retained at high α-doses. This will also be detrimental for larger ions such as caesium (although decay timescales must be considered in the context of escape to the geosphere). In contrast, assuming a randomly oriented crystallite breakdown mechanism for damage accumulation,

an increase in available 'edge' sites will be beneficial to the crystal's sorption capacity up to a certain threshold. Further work on damaged mineral sorption and reactivity is required. It is likely that edge site sorption will be more important than interlayer uptake in this context (Sawhney, 1972), particularly for uranium.

Reduction of the solid phase iron as a result of irradiation (discussed earlier) may be advantageous in a disposal case. Brookshaw et al (2013, 2014) observed considerable enhancement in cation uptake (and consequent reductive transformation) by bio-reduced phyllosilicates; whilst net reduction in this study is not on the same scale as bio-reduction, redox mechanisms clearly will have a crucial role in GDF models. Fe(II) in sorbing minerals can reduce edge sited uranium from the mobile uranyl $[U(VI)O_2]^{2+}$ cation to its immobile U(IV) oxidation state (Ilton et al., 2004; Myllykyla, 2008). Indeed, electron hopping along the octahedral plane (Fe sublattice) has been proposed to reduce uranyl (or similar) sorbed to edge sites in annite, thereby Fe^{2+} at 'deeper' sites within the structure can still influence redox activity at the near-surface of a crystal (Rosso & Ilton, 2003, 2005), which provides an Fe reduction mechanism by α-particle damage at depth in a crystal. With increasing dose however, any perceived 'benefits' of Fe reduction by α-particles may be lost as the mica loses its structure entirely, depending on the sorption capacity of highly damaged regions. Extensive further work on the effect of radiation damage on sorption to sheet silicates with subsequent reductive precipitation is underway.

Biotite mica is clearly highly susceptible to chemical and structural aberrations as a result of high fluence α-particle bombardment. Indeed, at the maximum dose delivered in this study (~ 6.8 dpa) amorphous areas dominate the structure; the crystalline regions that remain are heterogeneously distorted over areas < 60 μm. Whilst mica phases like biotite are unlikely to experience a near-field radiation dose, the structure shares important parallels with the phyllosilicate bentonite (comprising dominantly montmorillonite), which forms a crucial component of the engineered barrier system in a GDF to protect the waste container against corrosion and limit the release of radionuclides. A limiting

factor for using mica as a proxy for bentonite is the expandability of clay phases with increased hydration; a property not shared by micas excepting under weathering reactions ('hydrobiotite' consists of interstratification of biotite and its hydrated alteration product, vermiculite (Brindley, 1983)). Despite this, many of the structural aberrations that biotite mica undergoes during α-particle irradiation will be shared by layered clays; chiefly interlayer collapse, increased mosaicity and the potential for Fe(III) reduction. Indeed, Ferrage et al., (2005) comment that a thermal 'plume' surrounding waste canisters in the short term may cause smectite (a 2:1 expandable clay) to transform into non-expandable illite. Further radiation damage studies of both hydrated and dehydrated clay systems are needed to full understand their changing properties and performance in a developing GDF.

Whilst many radiation damage models display bulk, time averaged lattice responses to increased point defect densities; the data presented here demonstrates the necessity to consider the micro-scale spatial evolution of radiation damage as a result of both heterogeneous ion bombardment, which is of particular relevance when considering canister rupture and the subsequent complex irradiation effects on the buffer material and the heterogeneous nature of the resulting damage. α-particles are not the only radiation field present in the near-field of a GDF; combined irradiation studies (α,γ and heavy ions to simulate α-recoil from adsorbed actinides) upon similar structures are currently underway.

Acknowledgements

The authors are extremely grateful for the high quality sample sectioning and preparation throughout the project performed by Stephen Stockley, University of Manchester. WRB acknowledges NERC for funding under the DTA grant scheme awarded to the University of Manchester (code NE/K500859/1). The authors are also grateful to the Diamond Light Source, UK for analysis time on beamlines I18 and B18 (Beamtime award nos: SP9044, SP9647, SP9598) and invaluable project assistance. The Dalton Cumbrian Facility is a joint endeavour by the U.K. Nuclear Decommissioning Authority and the University of Manchester and its construction and commissioning was supported by both bodies. Spotlight™ 400 FTIR and Bruker D8 XRD data were collected in the University of Manchester's Williamson Research Centre and the authors acknowledge John Waters for assistance with XRD data collection. The authors gratefully acknowledge Steve Heald (Advanced Photon Source, Argonne National Lab) for providing the wüstite and hematite Fe K-edge XANES data. JP McKinley acknowledges support for the EPMA analyses from the Geochemistry Group at Pacific Northwest National Laboratory.

References

Allard, T., and Calas, G. (2009) Radiation effects on clay mineral properties. Applied Clay Science, 43, 143–149.

Ames, L.L., McGarrah, J. E, and Walker, B.A (1983) Sorption of uranium and radium by biotite, muscovite and phlogopite. Clays and Clay Minerals, 31, 343–351.

Biro, L.P, Gyulai, J., and Havancsak, K. (1997) Comparison of damage produced by 209MeV Kr irradiation in muscovite mica, graphite and silicon. Nuclear Instruments and Methods in Physics Research B, 122, 476–480.

Bower, W.R., Smith, A.D., Pattrick, R.A.D., and Pimblott, S.M. (2015) Establishing α-particle radiation damage experiments using the Dalton Cumbrian Facility's 5 MV tandem pelletron. Reviews of Scientific Instruments, 86, 046105.

Bower W. R., Pearce, C.I., Droop, G. T. R., Mosselmans, J. F. W., Geraki, K., Pattrick, .R .A D. (2015) Radiation damage from long term alpha particle bombardment of silicates - a microfocus XRD and Fe K-edge XANES study. Mineralogical Magazine, In Press

Chailley, V., Dooryhée, E., Bouffard, S., Balanzat, E., and Levalois, M. (1994) Observations by X-ray diffraction of structural changes in mica irradiated by swift heavy ions. Nuclear Instruments and Methods in Physics Research Section B: Beam Interactions with Materials and Atoms, 91, 162–167.

Chailley, V., Dooryhee, E., and Levalois, M. (1996) Amorphisation of mica through the formation of GeV heavy ion tracks. Nuclear Instruments and Methods in Physics Research B, 107, 199–203.

Chaussidon, J. (1971) The I.R spectrum of structural hydroxyls of K+ depleted biotites. Clays and Clay Minerals, 20, 59–67.

Dent, A.J., Cibin, G., Ramos, S., Smith, A.D., Scott, S.M., Varandas, L., Pearson, M.R., Krumpa, N.A., Jones, C.P., and Robbins, P.E. (2009) B18: A core XAS spectroscopy beamline for Diamond. Journal of Physics: Conference Series, 190, 012039.

Fialips, C. I, Huo, D., Yan, L., Wu, J., and Stucki, J.W. (2002) Effect of Fe oxidation state on the IR spectra of Garfield nontronite. American Mineralogist, 87, 630–641.

Fleet, M.E, and Deer, W.A. Howie, R.A. Zussman, J. (2003) Rock-forming Minerals: Micas, Second., 765 p. Vol. 3A. The Geological Society.

Holland, T.J.B., and Redfern, S.A.T (1997) Unit cell refinement from powder diffraction data: the use of regression diagnostics. Mineralogical Magazine, 61, 65–77.

Idemitsu, K., Obata, K., Furuya, H., and Inagaki, Y. (1995) Soroption behaviour of uranium (VI) on a biotite mineral. Scientific basis for nuclear waste management, 18.

Igor Pro (2014). WaveMetrics, Inc.

Ilavsky, J. (2012) Nika - software for 2D data reduction. J. Appl. Cryst., 45, 324–328.

Ilton, E.S., Haiduc, A., Moses, C.O., Heald, S.M., Elbert, D.C., and Veblen, D.R. (2004) Heterogeneous reduction of uranyl by micas: Crystal chemical and soliution controls. Geochimica et Cosmochimica Acta, 68, 2417–2435.

Leay, L., Bower, W., Horne, G., Wady, P., Pottinger, M., Nancekievill, M., Smith, A.D., Watson, S., Green, P.R., Lennox, B., and others (2015) Development of irradiation capabilities to address the challenges of the nuclear industry. Nuclear Instruments and Methods in Physics Research B, 343, 62–69.

Lee, S.Y., and Tank, R.W. (1985) Role of clays in the disposal of nuclear waste: A review. Applied clay science, 1, 145–162.

Lee, S.Y, Baik, M. H., Lee, Y. J., and Lee, Y. B. (2009) Adsorption of U(VI) ions on biotite from aqueous solutions. Applied Clay Science, 46, 255–259.

Lieser, K.H. (1997) Nuclear and Radiochemisty: Fundamentals and Applications, First. Vols. 1-1, Vol. 1. VCH.

Lockwood, G.K., and Garofalini, S.H. (2010) Effect of moisture on the self-healing of vitreous silica under irradiation. Journal of Nuclear Materials, 400, 73–78.

Lu, F., Huan, M., Yaqoob, F., Lang, M., Namavar, F., Trautmann, C., Sun, H., Ewing, C., and Lian, J. (2012) Displacive radiation-induced structural contraction in nanocrystalline ZrN. Applied Physics Letters, 101.

Mosselmans, J.F.W., Quinn, P.D., Dent, A.J., Cavill, S.A., Moreno, S.D., Peach, A., Leicester, P.J., Keylock, S.J., Gregory, S.R., Atkinson, K.D., and others (2009) I18 – the microfocus spectroscopy beamline at the Diamond Light Source. Journal of Synchrotron Radiation, 16, 818–824.

Myllykyla, E. (2008) Reduction of uranium in disposal conditions of spent nuclear fuel pp. 1–111. Working Report, Posiva.

Nasdala, L., Wenzel, M., Andrut, M., Wirth, R., and Blaum, P. (2001) The nature of radiohaloes in biotite: Experimental studies and modeling. American Mineralogist, 86, 498–512.

Nasdala, L., Wildner, M., Wirth, R., Groschopf, N., Pal, D.C., and Möller, A. (2006) Alpha particle haloes in chlorite and cordierite. Mineralogy and Petrology, 86, 1–27.

Nielsen, C. H. and Sigurdsson, H., (1981) Quantitative methods for electron microprobe analysis of sodium in natural and synthetic glasses, American Mineralogist, 66, 557-552

Palmer, D., and Conley, M. (1994) CrystalMaker. English, CrystalMaker Software Ltd.

Pattrick, R. A. D. Charnock, J. M., Geraki, T., Mosselmans, J. F. W., Pearce, C. I., Pimblott, S. and Droop, G. T. R. (2013) Alpha particle damage in biotite characterised by microfocus X-ray diffraction and Fe K-edge X-ray absorption spectroscopy. Mineralogical Magazine.

Ravel, B., and Newville, M. (2005) ATHENA, ARTEMIS, HEPHAESTUS□: data analysis for X-ray absorption spectroscopy using IFEFFIT. Journal of Synchrotron Radiation, 12, 537–541.

Reed, D.T, Donar, S.D, and Weiner, M.F (1987) Gamma and alpha radiation levels in a basalt high level waste repository: potential impact upon container corrosion and packing properties. Coupled Processes Associated with Nuclear Waste Repositories, 1, 325–338.

Rickwood, P.C. (1981) The largest crystals. American Mineralogist, 66, 885–907.

Rieder, M., Cavazzini, G., D'Yakonov, Y.., Gottardi, G., Guggenheim, S., Koval, P.., Muller, G., Neiva, A.M.., Radoslovich, E.., Robert, J.., and others (1999) Nomenclature of the micas. Mineralogical Magazine, 63, 267–279.

Rosso KM, and ES Ilton. 2003. "Charge transport in micas: The kinetics of FeII/III electron transfer in the octahedral sheet." Journal of Chemical Physics 119(17):9207-9218.

Rosso KM, and ES Ilton. 2005. "Effects of Compositional Defects on Small Polaron Hopping in Micas." *Journal of Chemical Physics* 122(24):244709

Savage, D., and Arthur, R. (2012) Exchangeability of bentonite buffer and backfill materials p. 57. STUK Radiation and Nuclear Safety Authority.

Sawhney, B.L. (1972) Selective sorption and fixation of cations by clay minerals: a review. Clays and Clay Minerals, 20, 93–100.

Stadelmann, P. (2012) Jems Electron Microscopy Software.

Strobel, P., Durr, J., Tuilier, M.-H., and Charenton, J.-C. (1993) Extended X-ray absorption fine structure study of potassium and caesium phyllomanganates. J. Mater. Chem., 3, 453–458.

The MathWorks Inc. (2013) MATLAB R2013a.

Thermo Electron Corporation (2004) OMNIC.

Vedder, W. (1969) Dehydroxylation and rehydroxylation, oxidation and reduction of micas. American Mineralogist, 54, 482–509.

Wang, L.M., Wang, S.X., Gong, W.L., and Ewing, R.C. (1998) Temperature dependence of Kr ion-induced amorphization of mica minerals. Nuclear Instruments and Methods in Physics Research Section B: Beam Interactions with Materials and Atoms, 141, 501–508.

Wilkins, R.W.T (1967) The hydroxl-stretching region of the biotite mica spectrum. Mineralogical Magazine, 36, 279–325.

Wolfer, W.G. (2000) Radiation effects in plutonium: What is known? Where should we go from here? Los Alamos Science, 26, 274.

Ziegler, J.F. (2013) The Stopping and Range of Ions in Matter (SRIM).

Figure Captions

Figure 1. CrystalMaker (Palmer, D. and Conley, M. 1994) image of biotite mica structure, viewed along the phyllosilicate layers, illustrating the sequential arrangement of the TOT sheets. Large, potassium-rich interlayers create planes of weakness accounting for the micas perfect cleavage. OH^- groups (green label) occupy the voids between hexagonal silica rings and are oriented towards the octahedral layer. Samples were mounted such that incident ions penetrated across the parallel layers, as shown by the dashed arrow.

Figure 2. A. Optical photograph of a cleavage parallel plane of biotite mica, sectioned for analysis, following exposure to 9.2×10^{15} $^4He^{2+}$ ions across the beam profile in **B**. Note the mottled, silver discolouration of the irradiated area, marked by the dashed line. **B.** Cross-section through the Gaussian profile of the $^4He^{2+}$ ion beam footprint shown in Figure 2A. Solid black lines (sections **i**, **ii** and **iii**) represent areas selected for sequential XRD traverses (each with a track step of 30 µm as shown in Figure 4). Dashed black lines (section **iv**) display the area analysed at higher resolution (5 µm track steps), the dashed grey line indicates the ion beam limit, note that the area to the left of this line in panel **i** has not been irradiated.

Figure 3. Representative high resolution 2D X-ray diffraction patterns (CCD images) from across the irradiated biotite sample. Distances (µm) denote proximity from $^4He^{2+}$ ion beam centre, as illustrated in Figure 2. The upper left panel displays the calibration pattern taken from powdered silicon, on which three major reflections are marked (2θ angles).

Figure 4. Transmission X-ray diffraction 'map' displaying X-ray diffraction angle changes (2θ) across the [001] oriented biotite, plotted as a function of distance from the ion beam centre (0 µm denotes height of beam intensity, see Table 2). The dashed line denotes the limit of the ion beam, below which the sample has not been irradiated. Panels **i – iv** represent areas displayed in Figure 2 and correspond to relative changes in beam intensity across the Gaussian beam profile. Panels **i, ii** & **iii** show a 7000 µm trace with diffraction patterns collected at 30 µm intervals, whilst panel **iv** denotes a 300 µm trace with patterns collected at 5µm intervals over a region of interest (4000-4300 µm).

Figure 5. 1D X-ray diffraction patterns showing the changes in peak position and intensity as a function of ion beam dose. Patterns have been selected at 1000µm intervals across the traverse shown in Figure 4**.** Dotted lines display the reduced 1D data from the CCD images, solid lines represent fitted peaks overlaid onto the 1D data.

Figure 6. Relative changes in *a* and *b* lattice dimensions of irradiated biotite as a function of distance from beam centre (0µm represents maximum dose) calculated using *UnitCell* (Holland and Redfern, 1997).

Figure 7. A. Representative *basal plane parallel,* 1D diffraction patterns at increasing depths into the sample from the irradiated surface of the crystal. Dotted lines display the reduced 1D data from the CCD images, solid lines represent fitted peaks overlaid onto the 1D data. **B.** SRIM modeling predicts that $^{4}He^{2+}$ ions have a penetration distance of 18µm in biotite mica, thus patterns at 25 and 30 µm are assumed to be unirradiated. The bar chart shows simulated knock-on displacements caused by incident $^{4}He^{2+}$ ions into model biotite density and chemistry (simulations do not account for mineral structure). The highest displacement density occurs between 15-20µm (with a peak at 18µm) as the incident ions lose enough energy to permit structural interaction within the target. Simulations were run using SRIM (Ziegler, 2013).

Figure 8. Single crystal X-ray diffraction patterns acquired with a Bruker D8 CuKα lab source across two irradiated biotite samples and one standard. Δd denotes the change in d spacing (Å) between the unirradiated (0 dpa) and the highest dose (0.18 dpa) patterns for each plane. Due to the nature of the prepared cleavage parallel samples, only reflections parallel to the phyllosilicate layers were acquired. Dotted lines display the 1D data, solid lines represent fitted peaks overlaid.

Figure 9. A. Fe-K edge X-ray absorption near edge spectra of irradiated (~2000 μm from $^{4}He^{2+}$ beam centre) and unirradiated biotite, spaced for clarity. Note the ~2eV energy shift of the absorption edge following exposure to the ion beam.

Figure 10. Iron K-edge Extended X-ray Absorption Fine Structure (EXAFS) oscillations (k^3) for biotite irradiated with sequentially increasing fluences of $^{4}He^{2+}$ ions. Black solid lines show the EXAFS oscillations whilst red dashed lines display the fit to the data. Adjacent is the non phase-corrected Fourier transform magnitude for each of the corresponding EXAFS plots with fits (A-F). All spectra have been spaced for clarity.

Figure 11. Potassium *K*-edge edge X-ray Absorption Near Edge Spectra (XANES) for both unirradiated and irradiated biotite. Inset is the non phase-corrected Fourier transform magnitude for the corresponding spectra, note the slight contraction of the first and second 'shells'.

Figure 12. Intensity-normalized Fourier transform infra-red absorption spectra, centred over the OH^- stretching region of unirradiated, heated and irradiated biotite.

Table 1. Irradiated sample details.

Sample	Current (nA)	Time (mins)	Ion fluence*	dpa**
1	160	324	$9.6x10^{15}$	0.28
2	100	288	$6x10^{15}$	0.18
3	75	175	$2x10^{15}$	0.06

*total accumulated $^{4}He^{2+}$ ions over the beam footprint (r = 6.6 mm)

** Displacements per atom calculated based on the average ion beam density over the beam spot, based on SRIM modeling and extrapolation of ion densities. Differences in dose across a single sample is shown in Table 2.

Table 2. Dose estimations across beam profile for sample 1.

Dist. from beam centre (µm)	Ion fluence*	dpa**
7000-6750	Unirradiated	0
6750-5750	$2.67x10^{13}$	0.01
5750-4730	$1.67x10^{14}$	0.02
4730-3720	$4.85x10^{14}$	0.10
3720-2700	$1.05x10^{15}$	0.20
2720-1690	$1.86x10^{15}$	0.40
1690-1010	$1.31X10^{15}$	0.70
1010-690	$1.49x10^{15}$	2.60
690-0	$3.20x10^{15}$	6.77

*total accumulated $^{4}He^{2+}$ ions over the area specified integrated over a 323 minute exposure to a ~200nA beam, estimated by on-sample current monitoring.

** Displacements per atom calculated based on the ion beam density within the area specified, note the differences in area width accounting for non-linear increase in dpa into the beam centre. Atomic displacement parameters for biotite calculated using SRIM (Ziegler, 2013).

Table 3. Fe *K*-edge EXAFS fit results for unirradiated and irradiated biotite. Dist. denotes approximate distance from the ion beam centre (height of α-particle fluence). CN denotes coordination number; R denotes interatomic distance; σ^2 denotes Debeye-Waller factor; $S0^2$ denotes the amplitude reduction factor; *r* denotes the 'goodness of fit' factor. '*' denotes a fixed parameter.

Dist. (μm)	Spectrum	Path	CN	R (Å)	σ^2 (Å^2)	$S0^2$	*r*
Unirradiated	A	Fe-O	6.0*	2.07 ± 0.01	0.016 ± 0.001	0.90	**0.004**
		Fe-Fe	6.0*	3.11 ± 0.03	0.020*		
		Fe-Si	4.0*	3.38 ± 0.01	0.010 ± 0.002		
~ 3000 ± 100	B	Fe-O	6.0*	2.10 ± 0.01	0.010 ± 0.001	0.70	**0.012**
		Fe-Fe	6.0*	3.12 ± 0.02	0.020 ± 0.005		
		Fe-Si	4.0*	3.40 ± 0.01	0.006 ± 0.002		
~ 2500 ± 100	C	Fe-O	6.0*	2.09 ± 0.01	0.013 ± 0.001	0.78	**0.006**
		Fe-Fe	6.0*	3.03 ± 0.03	0.020 ± 0.005		
		Fe-Si	3.0*	3.37 ± 0.01	0.010 ± 0.002		
~ 2000 ± 100	D	Fe-O	6.0*	2.11 ± 0.01	0.009 ± 0.001	0.70	**0.016**
		Fe-Fe	6.0*	3.12 ± 0.03	0.013 ± 0.005		
		Fe-Si	3.0*	3.39 ± 0.03	0.007 ± 0.002		
~ 1500 ± 100	E	Fe-O	6.0*	2.08 ± 0.01	0.013 ± 0.001	0.75	**0.006**
		Fe-Fe	5.0*	3.01 ± 0.03	0.030 ± 0.005		
		Fe-Si	3.0*	3.38 ± 0.02	0.010 ± 0.002		
~ 1000 ± 100	F	Fe-O	6.0*	2.11 ± 0.01	0.008 ± 0.001	0.75	**0.009**
		Fe-Fe	6.0*	3.12 ± 0.03	0.012 ± 0.005		
		Fe-Si	4.0*	3.39 ± 0.01	0.005 ± 0.002		

Table 4. Formula-normalized major element results of the EPMA traverse into the irradiated biotite (Std error ± 0.02). 'Dist.' represents the distance from the centre of the ion beam spot (peak of radiation damage). The point identified by a '*' denotes the limit of the ion beam as marked by the colour change on the biotite surface. 'Total' denotes the sum of all cations. The sum of Na + K has also been expressed for charge balance illustration (see text for further details).

Dist. (mm)	Al	Fe^{TOT}	Si	Ti	Na	Mg	K	Total	Na + K
9.0	2.35	2.46	5.48	0.37	0.03	2.96	1.95	15.60	1.99
8.5	2.45	2.54	5.27	0.37	0.04	3.13	1.98	15.78	2.02
8.0	2.41	2.46	5.43	0.36	0.04	2.99	1.94	15.63	1.98
7.5	2.39	2.48	5.45	0.36	0.03	2.97	1.93	15.61	1.96
7.0	2.47	2.48	5.41	0.36	0.03	2.92	1.94	15.61	1.97
6.5	2.45	2.46	5.42	0.35	0.02	2.99	1.93	15.62	1.96
***6.0**	2.50	2.46	5.34	0.36	0.03	3.02	1.96	15.67	1.99
5.5	2.44	2.43	5.46	0.37	0.02	2.93	1.91	15.56	1.93
5.0	2.37	2.41	5.58	0.35	0.03	2.85	1.88	15.48	1.91
4.5	2.41	2.43	5.51	0.36	0.04	2.88	1.91	15.53	1.95
4.0	2.43	2.46	5.46	0.35	0.03	2.93	1.91	15.58	1.94
3.5	2.27	2.42	5.60	0.36	0.04	2.92	1.91	15.51	1.95
3.0	2.36	2.40	5.63	0.36	0.04	2.78	1.85	15.42	1.89
2.0	2.34	2.43	5.60	0.36	0.02	2.83	1.88	15.47	1.90
1.5	2.32	2.39	5.56	0.36	0.05	2.95	1.88	15.52	1.93
1.0	2.37	2.45	5.54	0.36	0.04	2.86	1.88	15.52	1.93
0.0	2.44	2.41	5.46	0.36	0.03	2.94	1.93	15.57	1.96

SUPPORTING INFORMATION

Linear Combination Fitting

Linear combination fitting (LCF) was performed using Athena, as part of the Demeter XAS data processing suite (Ravel & Newville, 2005). Hematite $Fe(III)_2O_3$ and Wüstite Fe(II)O standards were used for relative comparisons between the two XANES spectra presented in the main manuscript (Figure 9). Results are presented below; whilst there are errors in the fits, relative comparisons between the two spectra will be valid.

1. Standard Biotite

LCF fit of biotite_std_1.dat as flattened mu(E) from 7114.4808 to 7144.4808

Fit included 49 data points and 3 variables, and approximately 22.517 measurements
Weights sum to 1: yes
Weights forced between 0 and 1: yes
Overall e0 shift used: no
Noise added to data: 0
R-factor = 0.0069107
Chi-square = 0.08485
Reduced chi-square = 0.0018053

. standard	weight	e0
Fe(III) Fe2O3-Hematite	0.542 (0.048)	-1.637 (0.261)
Fe(II) FeO- Wüstite	0.458 (0.048)	4.986 (0.184)

. sum 1.000

2. Irradiated Biotite

LCF fit of biotite_irradiated_1.dat as flattened mu(E) from 7111.5 to 7141.5

Fit included 72 data points and 3 variables, and approximately 22.517 measurements
Weights sum to 1: yes
Weights forced between 0 and 1: yes
Overall e0 shift used: no
Noise added to data: 0

R-factor = 0.0037686
Chi-square = 0.07826
Reduced chi-square = 0.0011342

.	standard	weight	e0
Fe(III)	Fe2O3-Hematite	0.369 (0.040)	-1.800 (0.279)
Fe(II)	FeO- Wüstite	0.631 (0.040)	2.560 (0.133)

. sum 1.000

Figure S1. Linear combination fit results for irradiated (above) vs standard (below) biotite. The irradiated spectra was collected at ~ 2000 µm from the centre of the $^{4}He^{2+}$ ion beam spot on sample 1. See corresponding Figures 9 & 10 in the main manuscript.

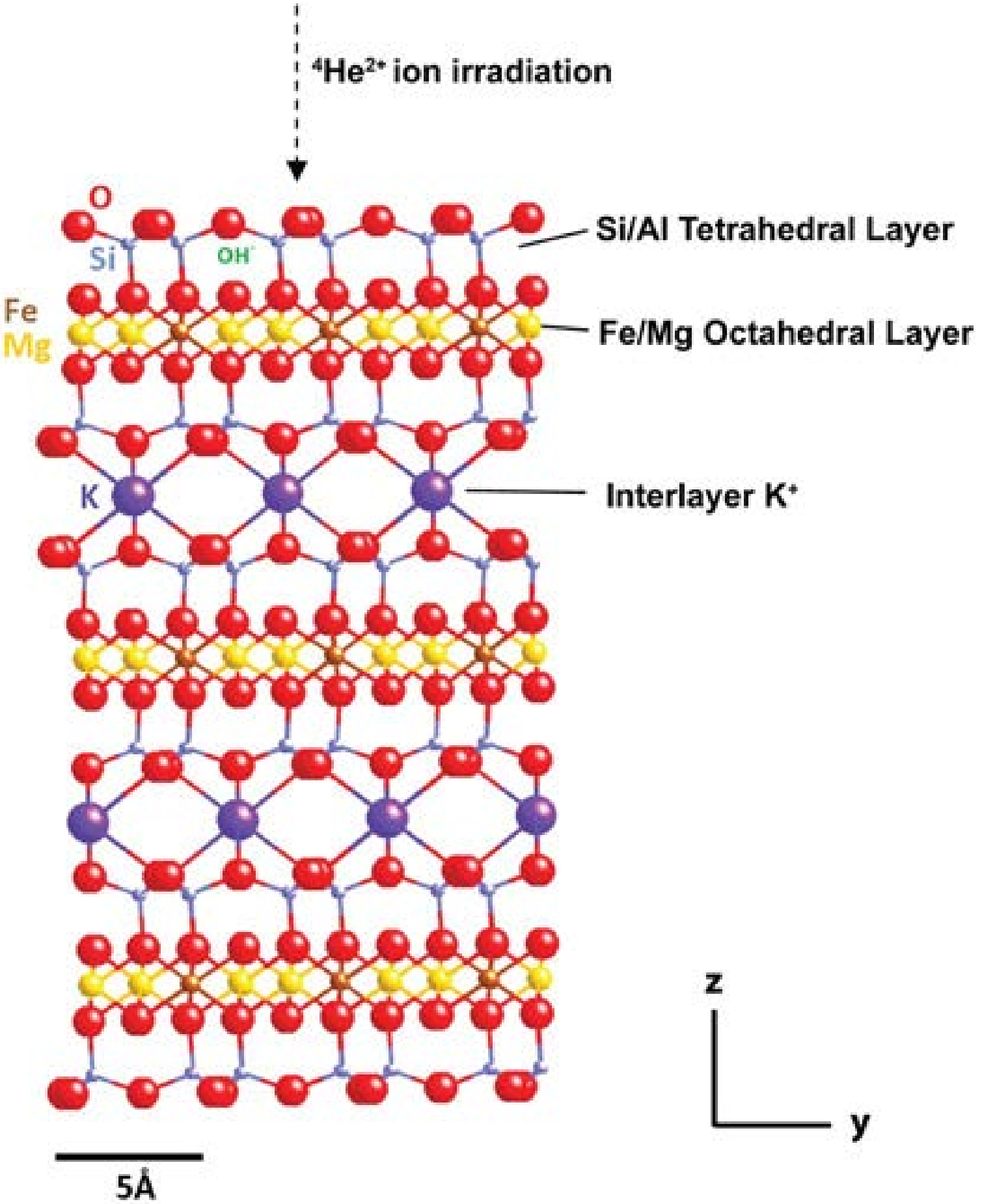
$^4He^{2+}$ ion irradiation
O
Si
OH⁻
Fe
Mg
K
Si/Al Tetrahedral Layer
Fe/Mg Octahedral Layer
Interlayer K⁺
z
y
5Å

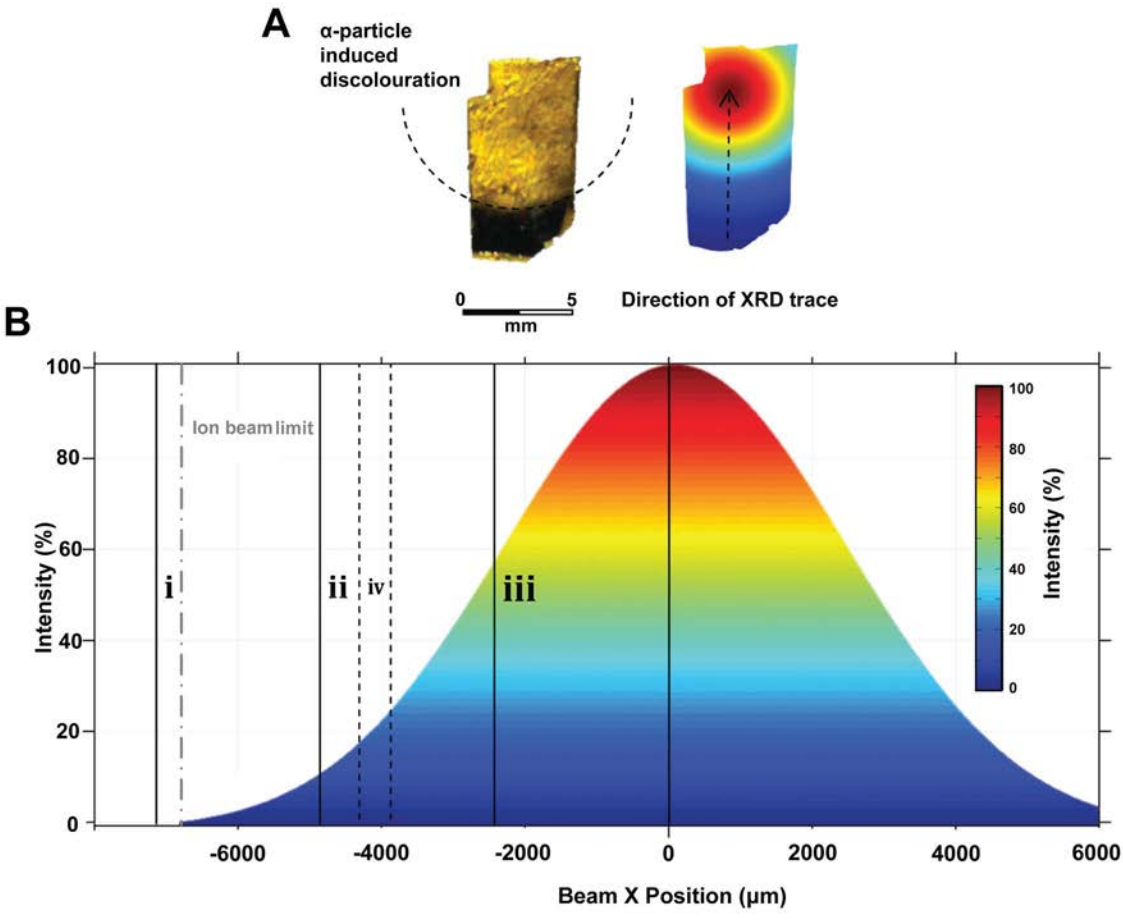
A
α-particle
induced
discolouration
0
5
mm
Direction of XRD trace
B
Ion beam limit
i
ii
iv
iii
Intensity (%)
Beam X Position (μm)
-6000
-4000
-2000
0
2000
4000
6000
0
20
40
60
80
100

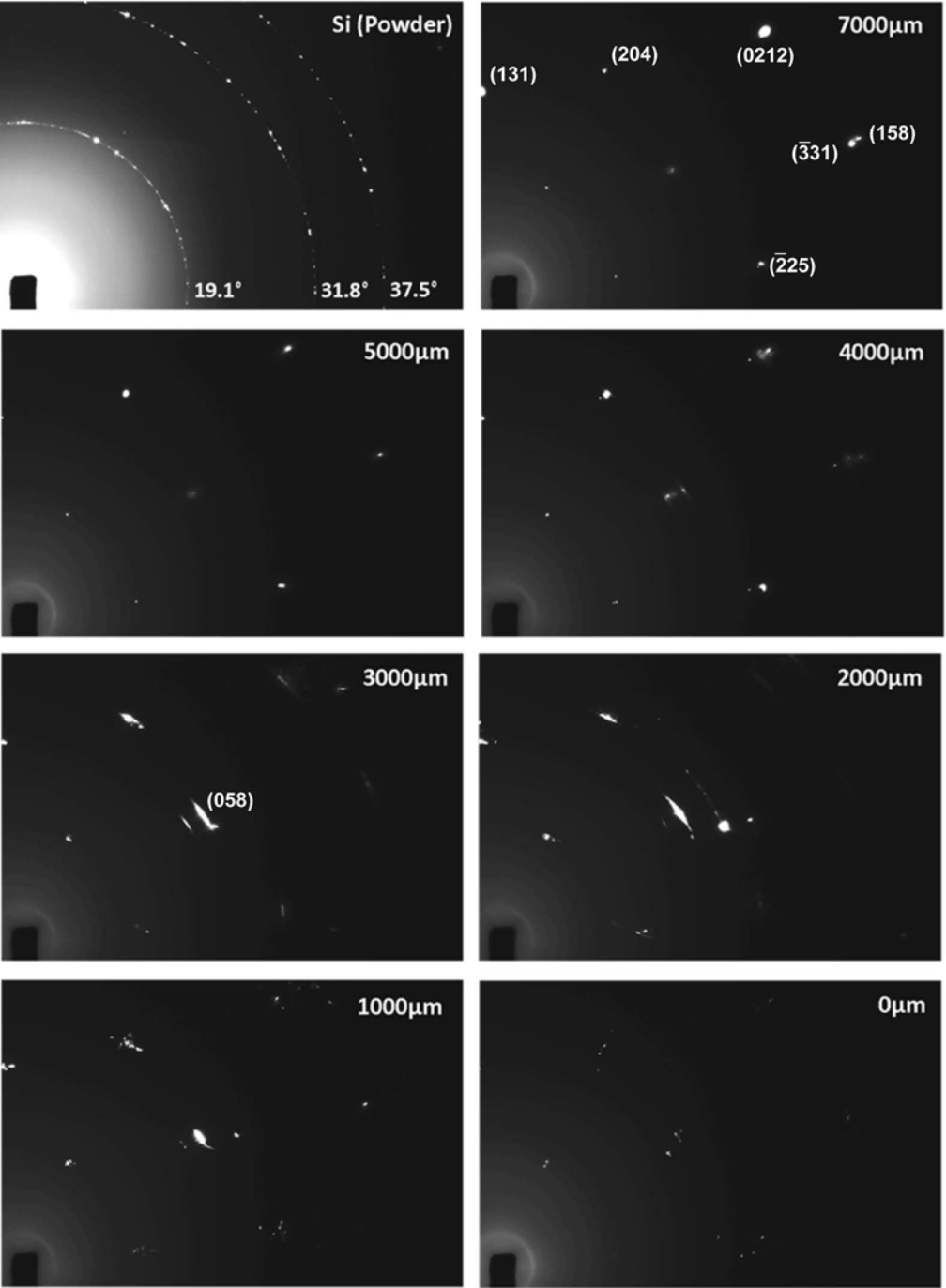
Si (Powder)
19.1°
31.8°
37.5°
7000µm
(131)
(204)
(0212)
(158)
($\bar{3}$31)
($\bar{2}$25)
5000µm
4000µm
3000µm
(058)
2000µm
1000µm
0µm

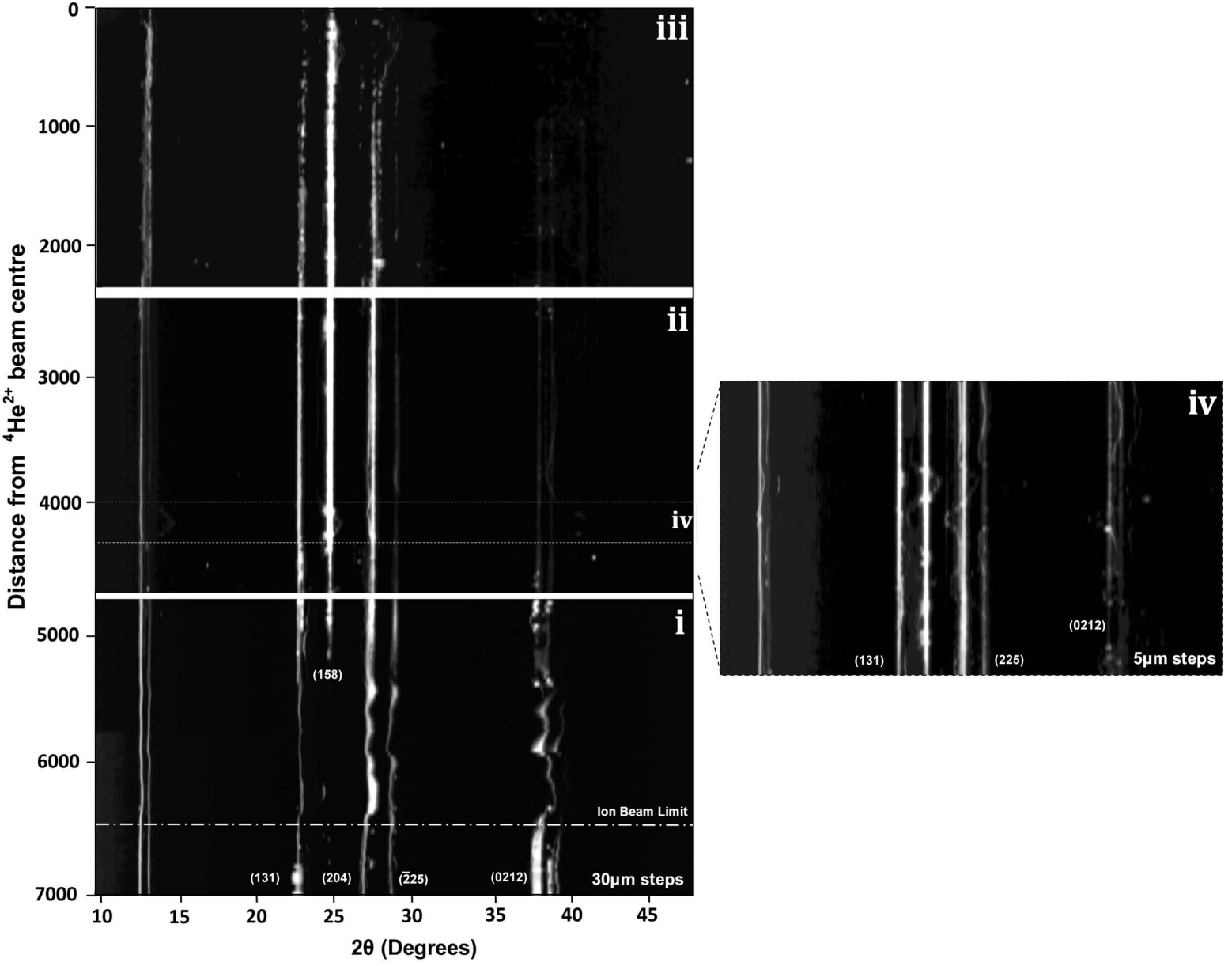
iii
ii
iv
i
(158)
Ion Beam Limit
(131)
(204)
(225)
(0212)
30μm steps
5μm steps
Distance from $^{4}He^{2+}$ beam centre
2θ (Degrees)
0
1000
2000
3000
4000
5000
6000
7000
10
15
20
25
30
35
40
45

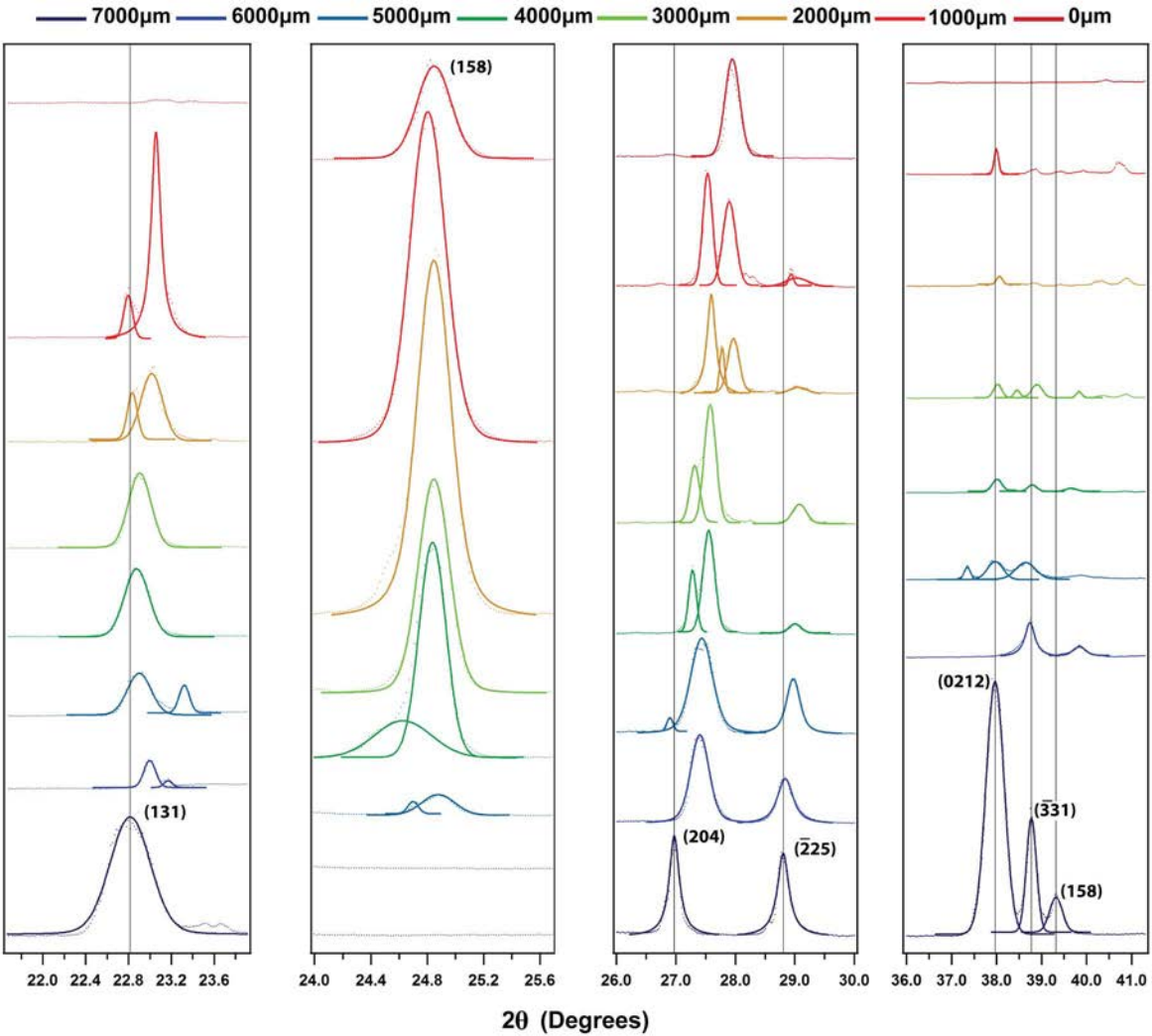
7000μm
6000μm
5000μm
4000μm
3000μm
2000μm
1000μm
0μm
(131)
(158)
(204)
(225)
(0212)
(331)
(158)
22.0 22.4 22.8 23.2 23.6
24.0 24.4 24.8 25.2 25.6
26.0 27.0 28.0 29.0 30.0
36.0 37.0 38.0 39.0 40.0 41.0
2θ (Degrees)

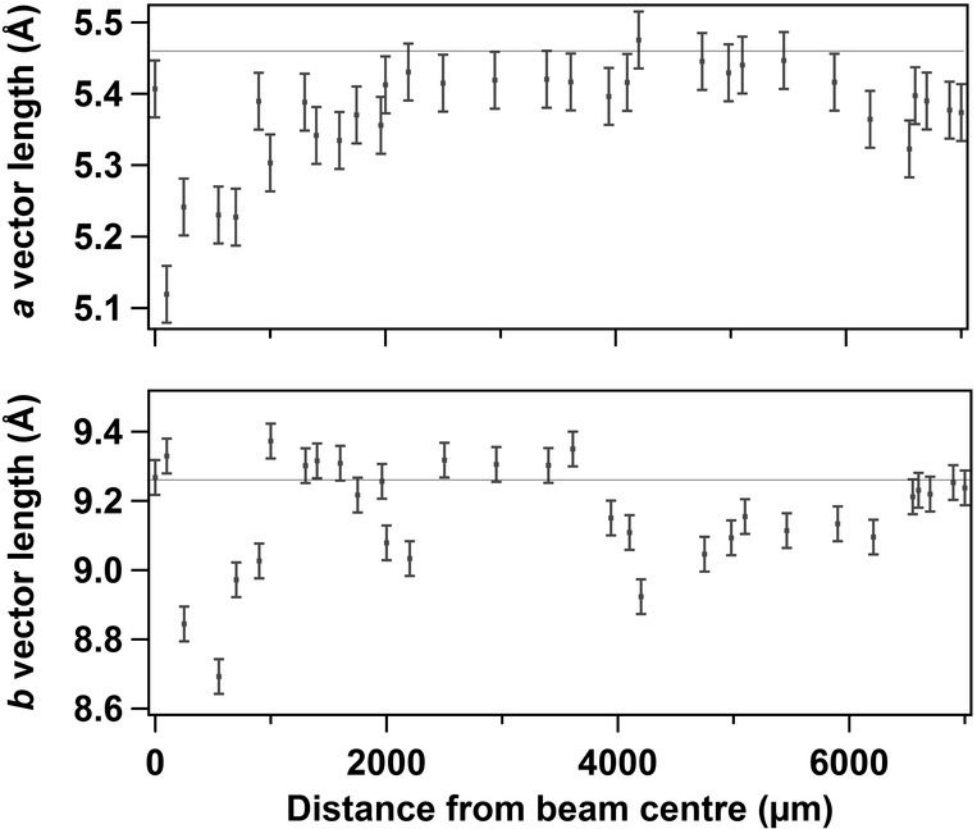
a vector length (Å)
5.5
5.4
5.3
5.2
5.1
b vector length (Å)
9.4
9.2
9.0
8.8
8.6
0
2000
4000
6000
Distance from beam centre (μm)

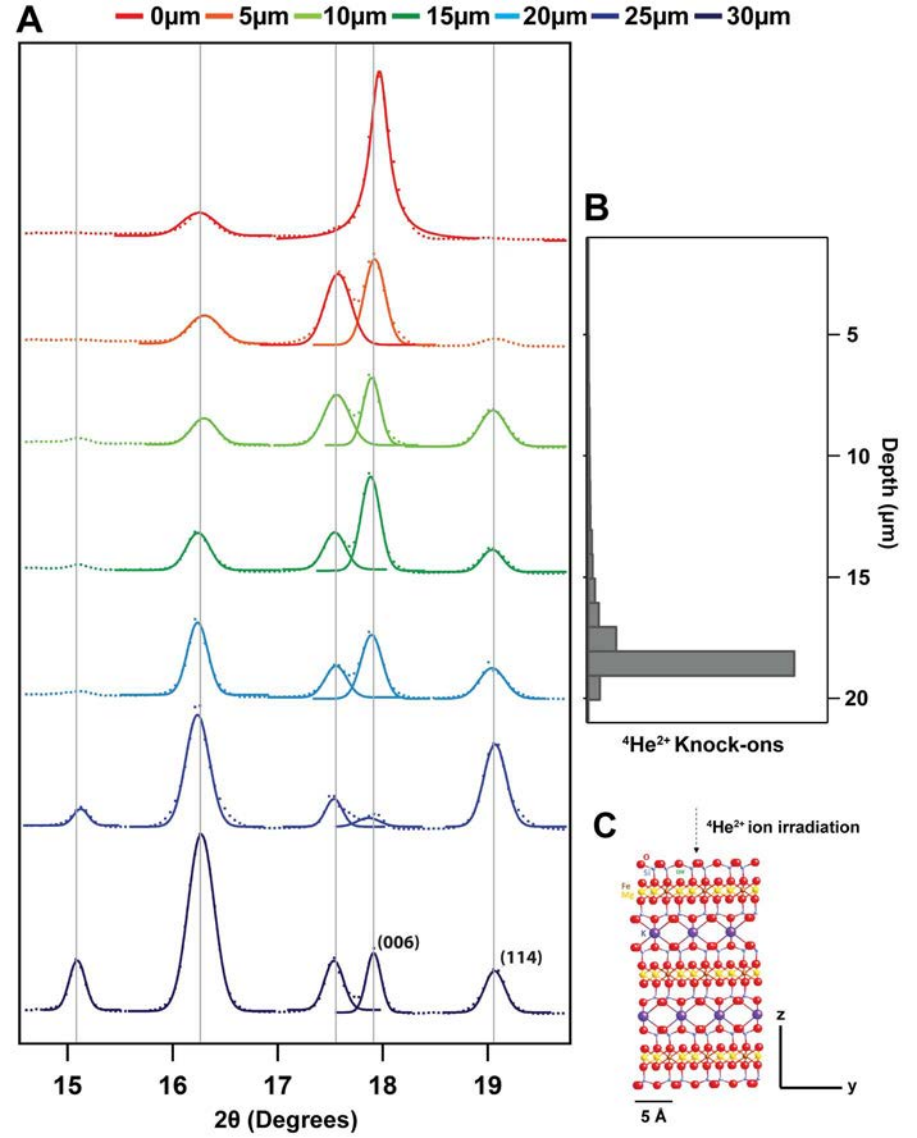
A
0μm
5μm
10μm
15μm
20μm
25μm
30μm
(006)
(114)
15
16
17
18
19
2θ (Degrees)
B
5
10
15
20
Depth (μm)
$^4He^{2+}$ Knock-ons
C
$^4He^{2+}$ ion irradiation
O
Bi
Sr
Cu
Fe
Se
K
z
y
5 Å

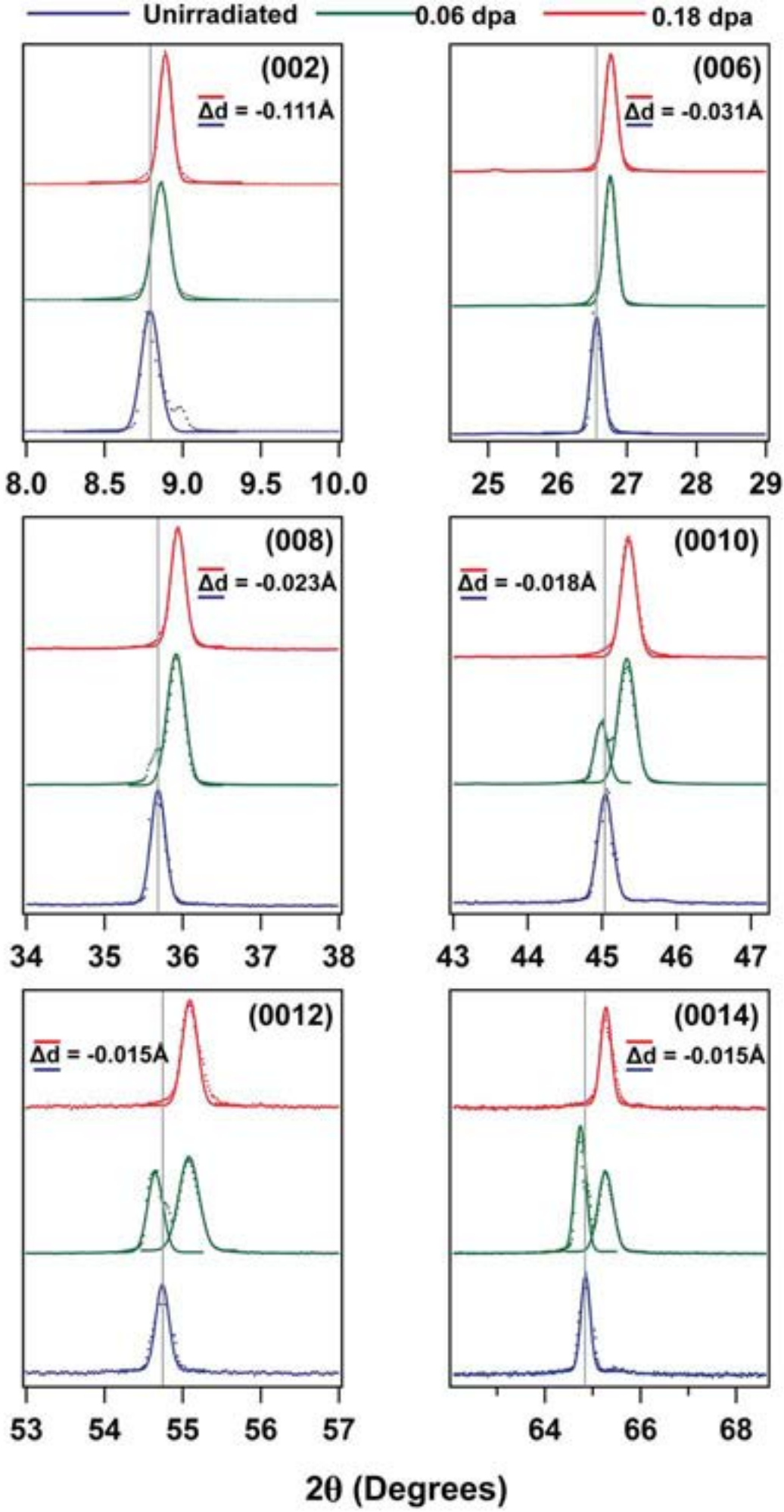
Unirradiated
0.06 dpa
0.18 dpa
(002)
Δd = -0.111Å
8.0
8.5
9.0
9.5
10.0
(006)
Δd = -0.031Å
25
26
27
28
29
(008)
Δd = -0.023Å
34
35
36
37
38
(0010)
Δd = -0.018Å
43
44
45
46
47
(0012)
Δd = -0.015Å
53
54
55
56
57
(0014)
Δd = -0.015Å
64
66
68
2θ (Degrees)

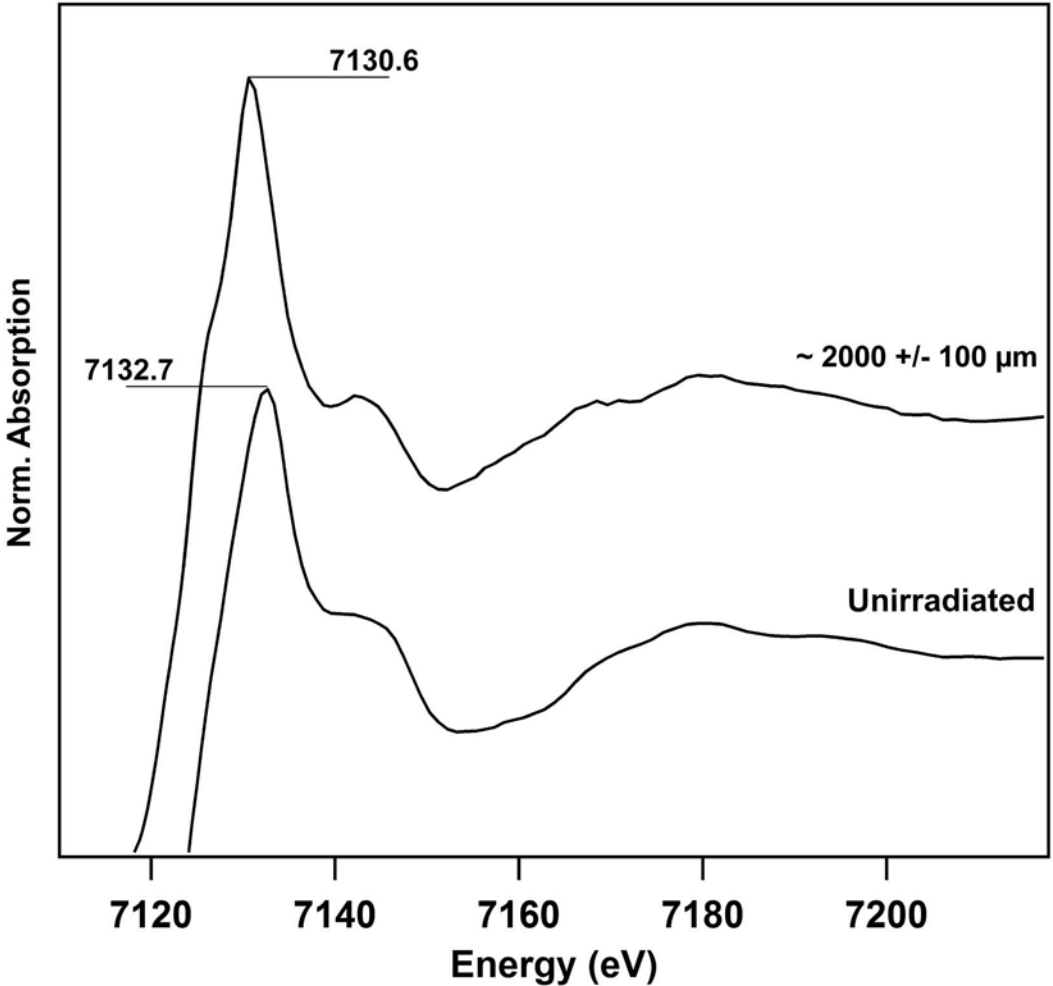
7130.6
7132.7
~ 2000 +/- 100 µm
Unirradiated
Norm. Absorption
7120
7140
7160
7180
7200
Energy (eV)

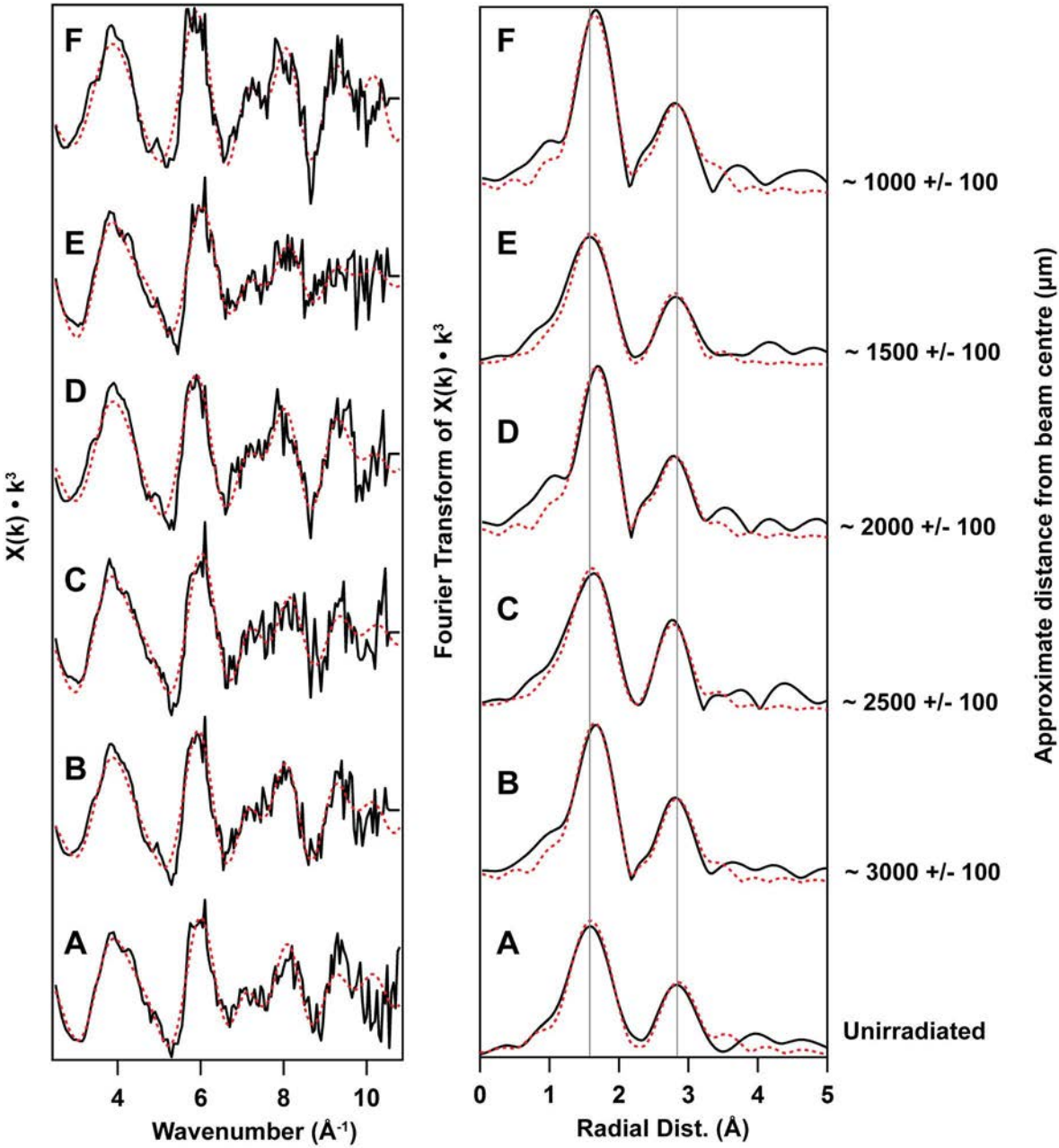
F
E
D
C
B
A
X(k) • k³
4
6
8
10
Wavenumber (Å⁻¹)
Fourier Transform of X(k) • k³
0
1
2
3
4
5
Radial Dist. (Å)
~ 1000 +/- 100
~ 1500 +/- 100
~ 2000 +/- 100
~ 2500 +/- 100
~ 3000 +/- 100
Unirradiated
Approximate distance from beam centre (µm)

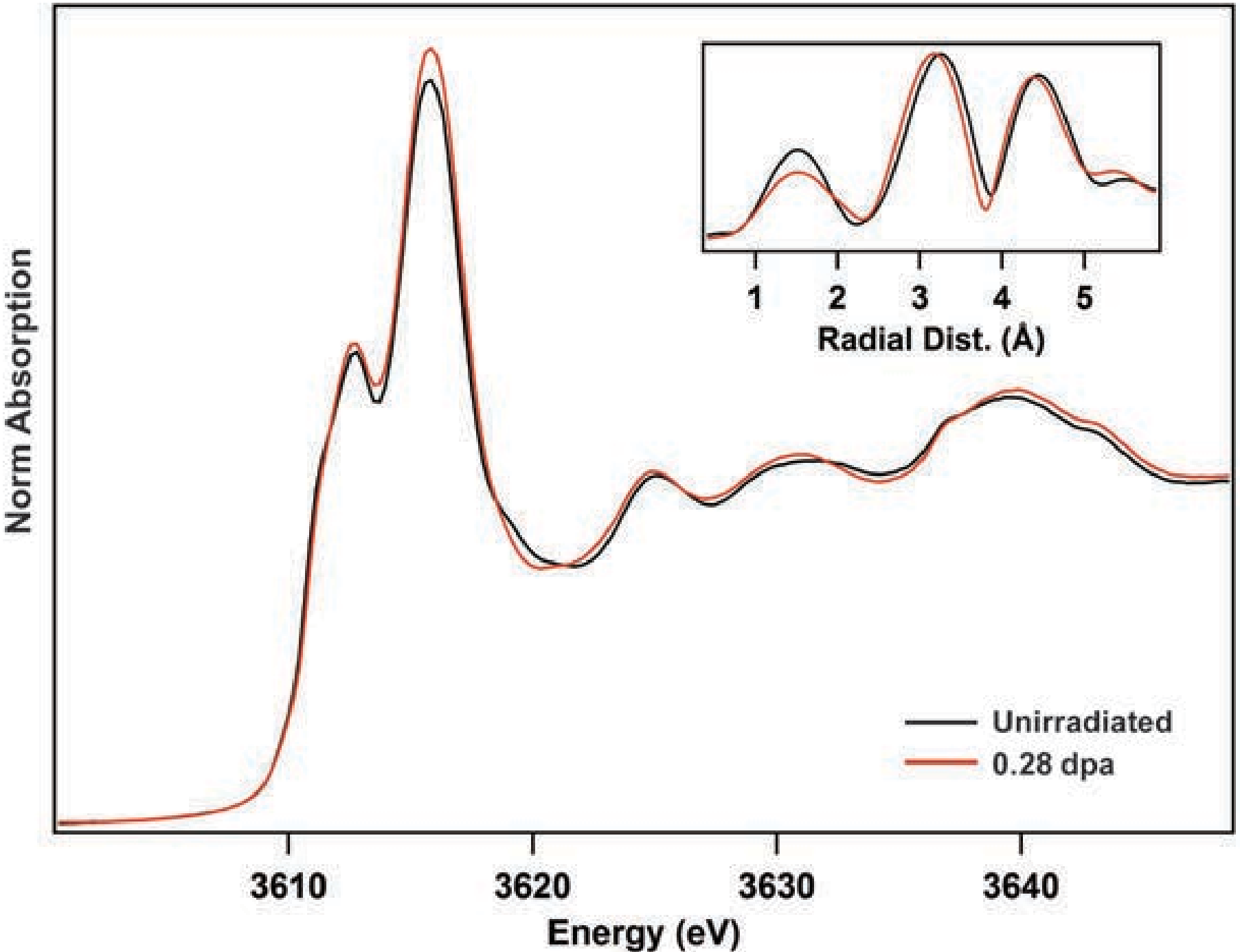
Norm Absorption
Energy (eV)
3610
3620
3630
3640
Radial Dist. (Å)
1
2
3
4
5
Unirradiated
0.28 dpa

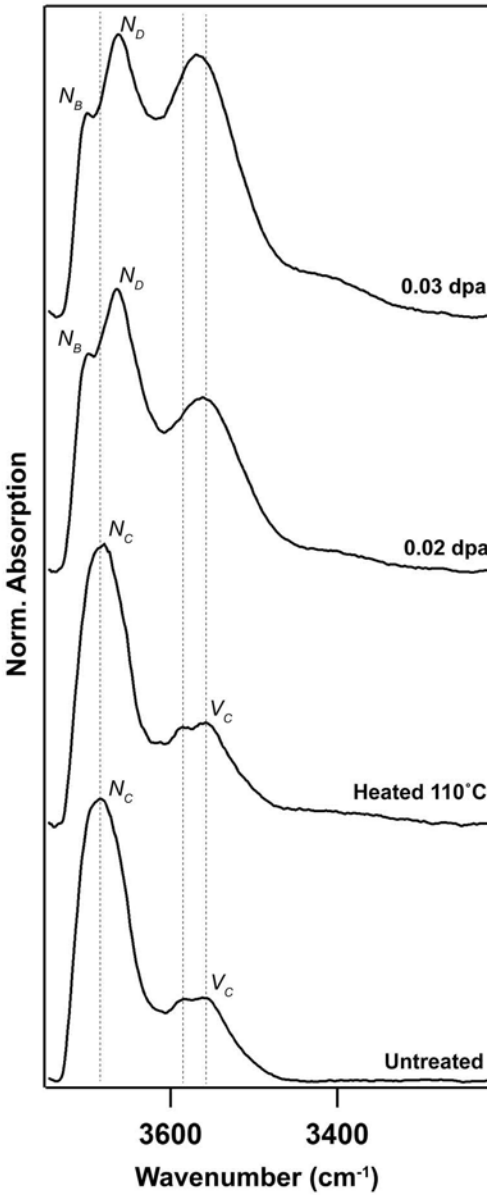
N_D
N_B
0.03 dpa
N_D
N_B
0.02 dpa
N_C
V_C
Heated 110˚C
N_C
V_C
Untreated
Norm. Absorption
3600
3400
Wavenumber (cm^{-1})